PISA-Net: A Physics-Informed Structure-Aware Neural Network for Multiphysics Field Reconstruction in Liquid Cooling Systems

Chaobo Zhang[1,†], Lizhe Jiang[2,3,†], Zhao Yang[1], Kun Yan[1,*], Jun Yan[2,*]

[1]Department of Chemical Machinery and Safety, School of Chemical Engineering, Dalian University of Technology, Dalian 116024, China

[2]Department of Engineering Mechanics, School of Mechanics and Aerospace Engineering, Dalian University of Technology, Dalian 116024, China

[3]BIM for Smart Engineering Centre, School of Engineering, Cardiff University, Cardiff CF24 3AA, UK

Highlights:

- Sparse sensors enable high-fidelity reconstruction of thermal–fluid fields.
- Hybrid physics–data modeling enhances accuracy and physical consistency.
- Structure-aware design adapts to varying heat source sizes.

Abstract: Efficient thermal management in liquid cooling systems relies heavily on the accurate reconstruction of temperature and velocity fields. However, obtaining full-field information under sparse sensor deployment remains a critical challenge. To address this issue, this study proposes a Physics-Informed Structure-Aware Network (PISA-Net) for adaptive and high-fidelity reconstruction of coupled thermal-fluid fields in liquid-cooled environments with limited measurements. The proposed framework integrates sparse temperature and velocity data with geometric information of heat sources and flow channels, enabling structure-aware representation of varying thermal configurations. A physics-informed loss term, derived from the steady-state energy conservation equation, is incorporated to enforce physical consistency during training. This hybrid learning strategy effectively combines data-driven approximation with physical constraints, improving both predictive accuracy and generalizability. Numerical validation on a representative cold plate configuration demonstrates that PISA-Net achieves a normalized mean absolute error of 0.98% for temperature and velocity field reconstruction using only eight sensor measurements. In addition, the

† These authors contributed equally to this work

* Corresponding author. E-mail address: yankun@dlut.edu.cn; yanjun@dlut.edu.cn

physics residual, quantified by the energy equation deviation, is reduced by approximately 80% compared to purely data-driven models. These results highlight the potential of PISA-Net as a robust and interpretable approach for real-time field reconstruction, anomaly detection, and sensor optimization in complex thermal-fluid systems.

Keyword: Liquid Cooling System; Thermal-fluid Fields Reconstruction; Sparse sensor measurements; Physics-Informed Neural Networks; Hybrid Data-physics Learning

Nomenclature

Roman symbols

p	Pressure	Pa
$Q(x, y)$	Distributed heat source	
q''	Surface heat flux	$W \cdot m^{-2}$
R	Radius of heat-source cylinder	mm
T	Temperature	K
$\hat{T}$	Predicted temperature (network output)	K
T_{in}	Inlet temperature	K
T_{out}	Outlet temperature	K
u, v	Velocity components in x- and y-directions	$m \cdot s^{-1}$
$\hat{u}$, $\hat{v}$	Predicted velocity components	$m \cdot s^{-1}$
$\vec{u} = (u, v)$	Velocity field	$m \cdot s^{-1}$
u_{in}	Fluid inlet velocity	$m \cdot s^{-1}$

Greek symbols

c_p	Specific heat at constant pressure	$J \cdot kg^{-1} \cdot K^{-1}$
k	Thermal conductivity	$W \cdot m^{-1} \cdot K^{-1}$
λ_0	Hyperparameter for weighting the data loss	
$\lambda_1(t)$	Hyperparameter for weighting the physical loss	
μ	Dynamic viscosity	$Pa \cdot s$
ρ	Density	$kg \cdot m^{-3}$
θ	Trainable parameters of PISA-Net network	

Model-related variables

$\mathcal{D}_s$	Sparse observations
$\mathcal{F}_\theta$	Deep neural network model (PISA-Net)
f_{global}	Global feature vector
f_i	Local feature vector
H, W	Domain height and width
$\mathcal{L}_{\text{data}}$	Supervised data-driven loss
$\mathcal{L}_{\text{PDE}}$	Physics-based loss from PDE residuals
$\mathcal{L}_{\text{total}}$	Total hybrid loss
$\mathcal{M}(x, y)$	Structure mask
$\mathcal{R}_{\text{energy}}$	Energy residual
T_i^s, u_i^s, v_i^s	Temperature and velocity data at sensor points
x_{init}	Initial upsampled global feature
x_{input}	Input tensor (global feature + mask)
Y	Ground-truth output (T, u, v)
Ŷ	Predicted output (T, u, v)
Abbreviations	
CFD	Computational Fluid Dynamics
CNN	Convolutional Neural Network
DeepONet	Deep Operator Network
FNO	Fourier Neural Operator
MLP	Multi-Layer Perceptron
NMAE	Normalized mean absolute error
PDE-R	Physical residual
PINN	Physics-Informed Neural Network
RMSE	Root mean square error
U-Net	U-shaped convolutional network

1. Introduction

The dense distribution of heat sources imposes stringent demands on the cooling efficiency and thermal reliability of thermal management systems [1, 2]. Liquid cooling technology has emerged as the mainstream solution for high heat flux thermal control systems, owing to its superior heat transfer capabilities, effective thermal capacity matching, and improved cooling uniformity [3-5].

Ensuring the thermal safety and long-term operational stability of such systems necessitates access to high-fidelity spatial distributions of temperature and velocity fields, which are essential for thermal anomaly detection and the development of intelligent control strategies [6, 7]. Despite their advantages, liquid cooling systems exhibit strongly coupled thermal-fluid behavior, where the temperature and velocity fields are interdependent and influenced by multiple factors, including internal heat source geometries and flow disturbances [8]. Consequently, reconstructing a single physical field is insufficient to fully characterize the system state. Instead, the simultaneous reconstruction of both temperature and velocity fields has become critical for achieving refined thermal regulation and enabling accurate multiphysics field analysis [9, 10].

In engineering applications, it is typically infeasible to obtain full-field information through direct visualization or measurement. Instead, only sparse temperature and velocity data can be acquired via a limited number of sensors. However, due to the sparse spatial distribution of these sensors, traditional reconstruction methods often struggle to accurately and efficiently infer the complete physical fields. As a result, the operation monitoring, state evaluation, and thermal management of liquid cooling systems often pose a typical physical inverse problem: reconstructing the complete internal temperature and velocity field distributions from limited measurement points [11, 12]. Such inverse problems are generally ill-posed, where the solution may lack existence, uniqueness, or stability [13, 14]. These challenges are further exacerbated under conditions involving complex geometries or incomplete boundary information, where conventional numerical or analytical methods often fail to produce stable and reliable reconstructions of the physical fields [15-17].

Classical physical field reconstruction methods can be broadly classified into two categories: direct interpolation methods and indirect inverse methods. Traditional direct approaches include techniques such as Kriging interpolation [18], radial basis function (RBF) interpolation [19], and spline interpolation [20]. While these methods can rapidly generate continuous fields between known measurements, their performance is highly dependent on the spatial coverage and distribution of observation points, and they typically exhibit low sensitivity to boundary conditions or structural variations. Indirect methods, by contrast, encompass state estimation and regularization-based inverse techniques. For example, Wei et al. [21] proposed a new sparse Kalman filtering method that can achieve force localization and reconstruction using a limited number of sensors. Liang et al. [22] applied Kalman filtering and dimensionality reduction to non-stationary image reconstruction in ultrasonic transmission tomography. These indirect methods can perform indirect inference by combining with system dynamics models, but they are generally highly sensitive to prior models and error distributions, have high computational complexity, and are difficult to be extended to applications involving complex flow fields with multiple structures [23, 24]. Therefore, achieving high-accuracy and generalizable reconstruction of temperature and velocity fields under sparse observation remains a key challenge in the intelligent thermal management of liquid cooling systems.

In recent years, the emergence of deep learning has opened new avenues for inverse problem modeling. Leveraging their powerful nonlinear approximation capabilities and end-to-end mapping structures, deep neural networks (DNNs) have been successfully applied to a wide range of inverse problems, including medical image reconstruction, electromagnetic inversion, and structural response identification [25-28]. In the field of thermal control, data-driven models can directly learn the mapping between sparse sensor measurements and target physical quantities. For instance, Chen et al. [29] constructed a network based on a transfer learning framework to achieve efficient identification of temperature responses and material parameters in thermal protection systems; Yan et al. [30] proposed a convolutional network architecture that successfully realized rapid reconstruction of the structural deformation field of aerospace vehicles under sparse observation conditions. Li et al. [31] put forward a data-driven model composed of a transposed network and a residual network to predict the flow field structure of supersonic cascade channels by measuring the wall pressure of the cascade channels. Gong and Wang [32] proposed an artificial neural network-based quadratic constitutive relation (ANN-QCR) for Reynolds stress modeling, incorporating field inversion and machine learning (FIML) techniques and high-fidelity experimental data for simulating separated turbulent flows. These approaches demonstrate high predictive accuracy and low computational cost when sufficient training data and stable operating conditions are available, making them promising tools for real-time monitoring, anomaly detection, and feedback control in thermal-fluid systems.

However, purely data-driven models inherently lack the capacity to incorporate explicit physical laws, often resulting in large reconstruction errors, severe overfitting, and limited generalization performance across varying conditions [33]. Consequently, incorporating physical priors into data-driven frameworks to enhance physical consistency and cross-structural robustness has emerged as a key focus of recent research efforts [34, 37]. To address this, Raissi et al. [38] proposed the Physics-Informed Neural Networks (PINNs) method, which realizes the embedded modeling of physical laws by explicitly introducing the residuals of control equations (such as convection-diffusion equations, Navier–Stokes equations) as loss terms in the training of neural networks. This method has achieved good results in tasks such as partial differential equation solving, parameter inversion, and dynamic prediction [39]. Despite these successes, PINNs face significant challenges in sparse observation problems. First, they typically require full-field spatial coordinates as inputs, which is incompatible with practical engineering conditions where only limited sensor measurements are available [40]. Second, training PINNs is often hindered by vanishing gradients [41] and optimization instability [42], especially in nonlinear strongly coupled systems, leading to poor convergence, long training times, and strong sensitivity to hyperparameter settings [43-45]. Third, PINNs generally lack explicit mechanisms to represent complex geometric boundaries, resulting in limited robustness in multi-structure or irregular domain reconstruction tasks [46-48].

In light of the aforementioned challenges, a key scientific and technical bottleneck in intelligent thermal management lies in developing a modeling framework that integrates data-driven learning with physical constraints to enable high-fidelity reconstruction of temperature and velocity fields under sparse sensor conditions, across diverse geometric structures and operating scenarios in liquid cooling systems. To address this issue, this study proposes a hybrid neural network framework - Physics-Informed Structure-Aware Network (PISA-Net) - which incorporates both structural awareness and physics-based constraints. The model takes sparse sensor measurements of temperature and velocity fields as input, and leverages structure masks to enhance perception of geometric and topological features. A physics-informed loss function based on the steady-state energy conservation equation is further introduced to enforce explicit physical consistency during training. By embedding physical priors within a data-driven architecture, PISA-Net significantly improves reconstruction accuracy and generalization across varying heat source configurations and sparse observation conditions.

The main contributions of this work are summarized as follows:

1) A hybrid neural network framework, PISA-Net, is proposed, which combines sparse sensor data with structural awareness via structure masks. The model enables high-fidelity reconstruction of temperature and velocity fields under varying operating conditions and geometric configurations.

2) A physics-informed loss function is designed based on the steady-state convection–diffusion energy equation and integrated into the training process to enforce physical consistency under weakly supervised conditions.

3) A finite element simulation dataset is established, covering diverse heat source structures and operating conditions, which serves as a high-quality benchmark for training and evaluating the proposed model.

The structure of this paper is organized as follows: Section 2 introduces the liquid cooling system and the mathematical description of the target problem. Section 3 presents the numerical analysis and dataset construction. Section 4 briefly describes the method of the proposed framework in this paper. Section 5 analyzes and discusses the results. Finally, some conclusions are given in Section 6.

2. Problem Formulation

This section provides a detailed description of the research problem and mathematically defines the considered problems.

2.1 Liquid Cooling System

In a typical design of multi-layer cold plate (MLCP), each layer of the cold plate is thermally coupled with heat-generating components, and several vertically aligned cylindrical elements are embedded within the structure. These elements act as localized heat sources or structural supports, while also inducing significant disturbances in the local flow field, as illustrated in Figure 1.

The liquid cooling system investigated in this study adopts a cold plate configuration. The channel thickness is considerably smaller than its length and width, and multiple cylindrical heat sources are embedded within the fluid domain to emulate the thermal behavior of electronic components or localized thermal loads. To reduce modeling complexity and improve computational efficiency, the three-dimensional thermal–fluid interaction problem is reasonably approximated as a two-dimensional inverse problem governed by steady-state nonlinear partial differential equations.

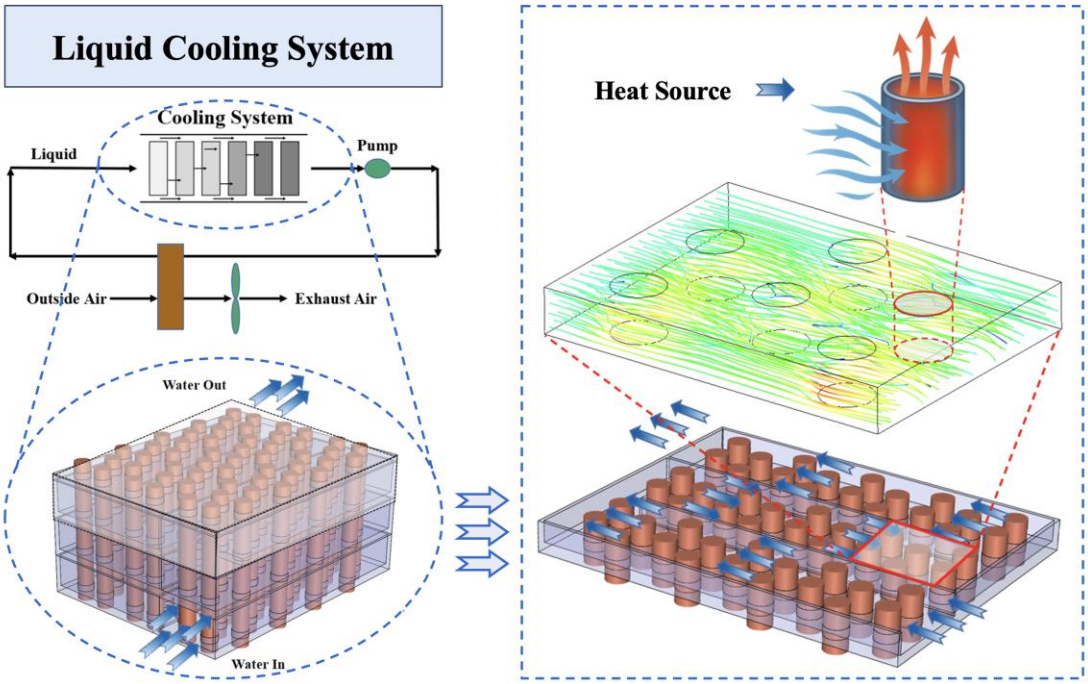

Figure 1. Liquid Cooling System

2.2 Problem Modeling

In liquid cooling systems, accurate knowledge of the internal temperature and velocity fields under operating conditions is essential. However, due to the high cost and potential impact on heat transfer performance, only a limited number of sensors can be deployed to capture temperature and flow velocity at discrete locations within the domain.

To address this limitation, this study employs deep learning techniques to construct a model that maps sparse sensor measurements to full-field physical quantities, as Figure 2.

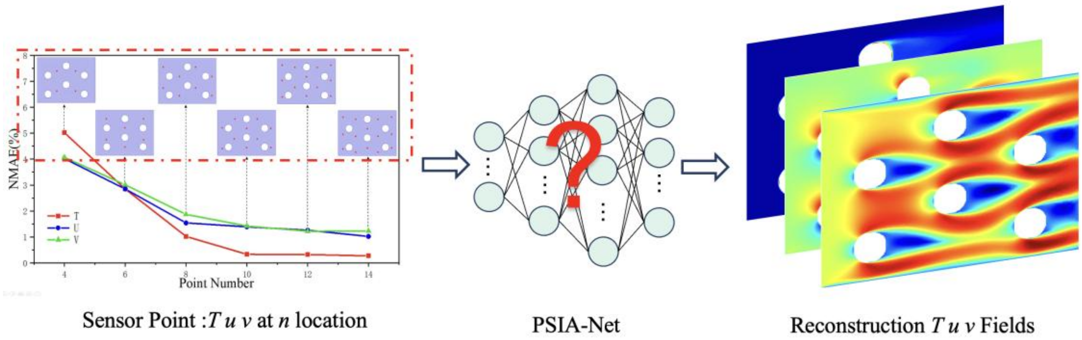

Figure 2. Problem Description

Given a set of sparse observations:

$$\mathcal{D}_s = \{(x_i, y_i, T_i^s, u_i^s, v_i^s)\}_{i=1}^{N} \tag{1}$$

the objective is to predict the corresponding continuous fields of temperature and velocity:

$$\mathcal{F}_\theta : \{(x_i, y_i), T_i^s, u_i^s, v_i^s, \mathcal{M}(x, y)\}_{i=1}^{N} \rightarrow \{T(x, y), u(x, y), v(x, y)\}_{(x,y)\in\Omega} \tag{2}$$

where, $\mathcal{F}_\theta$ denotes the deep neural network model (PISA-Net), parameterized by θ. The term, $\mathcal{M}(x, y)$ represents the geometric structure mask (i.e., a binary matrix that encodes the fluid domain corresponding to different structural configurations), and Ω is the two-dimensional design domain. The coordinates (x_i, y_i) indicate the positions of the sparse sensors, and (T_i^s, u_i^s, v_i^s) are the corresponding measured temperature and velocity components at those locations.

The goal is to learn the mapping $\mathcal{F}_\theta$ that accurately approximates the true physical fields $(T(x, y), u(x, y), v(x, y))$ based on the limited input $\mathcal{D}_s$ and structural prior $\mathcal{M}(x, y)$, thereby achieving high-fidelity and physically consistent reconstruction of the thermal–fluid fields.

3. Dataset Construction

3.1 Analysis Model

In this study, a two-dimensional planar model is established to represent a single layer of the cold plate. A rectangular fluid subdomain containing six representative cylindrical heat sources is extracted as the computational domain. This subdomain captures essential physical phenomena, including velocity recirculation and temperature gradient variations induced by the embedded heat sources, while significantly reducing the computational cost compared to full-system modeling. As such, it provides a balanced modeling strategy that ensures both physical fidelity and numerical efficiency. As illustrated in Figure 3, the two-dimensional rectangular cooling channel (128 mm × 96 mm) incorporates six embedded cylindrical structures with fixed spatial locations. The radius of each cylinder is treated as a tunable geometric parameter to simulate structural variations. Each cylinder is modeled as an internal heat source subjected to a constant heat flux boundary condition.

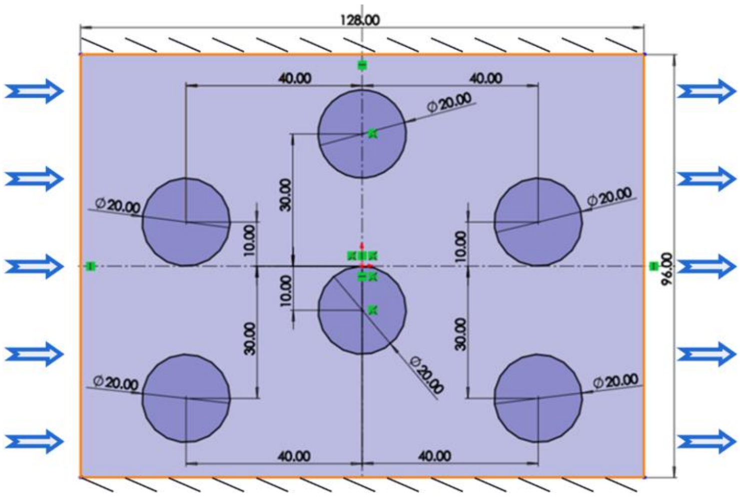

Figure 3. Structure Modeling

In the model, the geometric dimension of the heat source (characterized by radius R) is defined as a tunable parameter to reflect structural variations arising from different packaging configurations or design scales. The fluid inlet velocity U_{in} and inlet temperature T_{in} are specified as boundary condition variables, representing the level of flow enhancement and the thermal state of the incoming coolant, respectively. Meanwhile, the heat source intensity Q_{in} is treated as an internal condition variable, used to simulate the thermal load generated by the heat source under varying operational scenarios.

The coupled heat and flow behaviors under the system's steady state satisfy the following governing equations simultaneously:

Mass equation:

$$\nabla \cdot \vec{u} = 0 \tag{3}$$

Momentum equation:

$$\rho(\vec{u} \cdot \nabla)\vec{u} = -\nabla p + \mu \nabla^2 \vec{u} \tag{4}$$

Energy equation:

$$\rho c_p(\vec{u} \cdot \nabla T) = \nabla \cdot (k \nabla T) + Q(x, y) \tag{5}$$

Here, $\vec{u} = (u, v)$ represents the velocity field, p denotes pressure, and T signifies temperature. ρ, μ, c_p, k correspond to density, dynamic viscosity, specific heat capacity at constant pressure, and thermal conductivity respectively. $Q(x, y)$ indicates the distributed heat source term.

The energy equation adopted in this study is established under the steady-state assumption and neglects viscous dissipation.

This setting is consistent with the characteristics of the forced-convection liquid cooling plate investigated here, where the inlet velocity and temperature remain constant, and all CFD datasets were exported after steady convergence.

Under such conditions, the temporal variation of temperature becomes negligible compared to spatial gradients, making the steady-state energy balance appropriate for both the numerical simulations and the neural network reconstruction.

Furthermore, the viscous dissipation term, which represents the conversion of mechanical energy into internal energy due to shear stress, is several orders of magnitude smaller than the dominant convective–diffusive transport in low-Mach, laminar liquid-cooling flows.

Therefore, its omission introduces no measurable effect on the predicted thermal field and is a standard simplification for such operating regimes.

If the framework were to be extended to high-speed or high-viscosity cases, this term could be reintroduced without modifying the overall model structure.

The boundary conditions of the simulation domain are defined as follows:

1) The left inlet boundary is prescribed with varying combinations of inlet velocity u_{in} and inlet temperature T_{in}.
2) The right outlet boundary is set as a constant pressure outlet.
3) A constant heat flux q'' is applied to the cylinder to simulate the heat-generating source.
4) The top and bottom walls are modeled as adiabatic boundaries, implying zero heat flux.

The steady-state coupled solution of the incompressible Navier-Stokes equations and the energy conservation equation is conducted using Fluent for simulation.

3.2 Parameter Space and Sample Generation

To comprehensively evaluate the performance and generalization ability of the proposed method under varying heat source geometries and boundary conditions, a multiphysics dataset is constructed by sampling an extensive parameter space. Four categories of key physical parameters are selected for combination: the heat source radius R, surface heat flux q'', fluid inlet velocity u_{in}, and inlet temperature T_{in}. The discrete settings for each parameter are provided in Table 1:

Table 1. Structural and Operating Condition Parameters

Parameters	Intervals	Groups
R	5, 6, 7, 8, 9, 10 mm	6

q''	0.55×10^7–1.2×10^7 W/m²	5
u_{in}	0.01, 0.02, 0.03, 0.04, 0.05 m/s	5
T_{in}	283.15, 293.15, 303.15, 313.15 K	4

The selected parameters are designed to represent realistic operating conditions involving variations in heat dissipation intensity, flow disturbances, and geometric structures. To ensure both parameter space coverage and computational feasibility, a random sampling strategy is employed to uniformly select 300 representative combinations from the full factorial space for simulation and training purposes.

For each sampled condition, the simulation yields temperature (*T*) and velocity components (*u* and *v*), which are subsequently interpolated onto a uniform spatial grid and stored in a standardized format. The resulting dataset serves as the foundation for training and evaluating the proposed model, particularly in terms of its generalization capability across varying structural configurations and operating conditions.

3.3 Mesh Convergence of numerical model

Table 2 compares three levels of mesh resolutions in representative local regions, where the mesh with element size of 1mm achieves an effective trade-off between spatial resolution and computational cost. It also demonstrates excellent geometric conformity and numerical stability during simulation.

To ensure compatibility with the subsequent deep learning framework, all simulation results are uniformly interpolated onto a fixed spatial grid of size 193 × 257.

Table 2. Comparison of Mesh Convergence

Size	0.5mm	1.0mm	2.0mm
Mesh	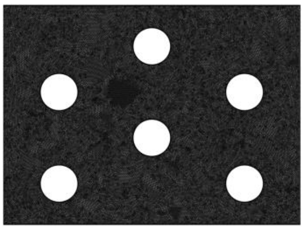	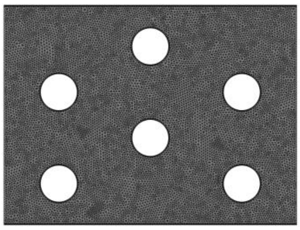	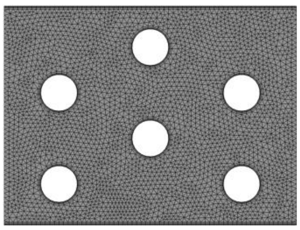
T	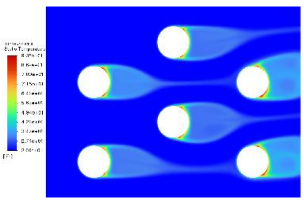	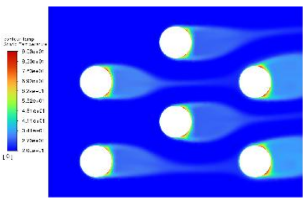	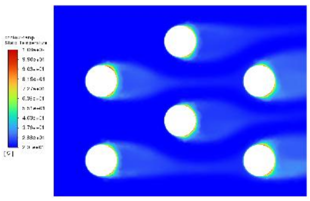

The CFD simulations were performed on unstructured triangular meshes. To obtain datasets with a uniform spatial resolution suitable for neural-network input, all simulation results were interpolated onto a regular Cartesian grid of 193 × 257 points covering the computational domain Figure 4. The interpolation is based on the finite-element shape-function reconstruction, which is mathematically equivalent to piecewise-linear interpolation within each triangular element. This approach ensures geometric flexibility for unstructured meshes and preserves the physical continuity and accuracy order of the numerical solution. Importantly, the interpolation was carried out only within the fluid domain. The circular solid regions corresponding to the cylindrical heat sources were excluded from the interpolation using a binary structural mask (mask = 0 for solid and mask = 1 for fluid). Consequently, the neural network processes and predicts physical fields (e.g., temperature, velocity) only in the fluid region, ensuring physical consistency and avoiding non-physical artifacts in the non-fluid domain. The generated uniform-field data and corresponding masks were then saved in .csv or .npy format for model training.

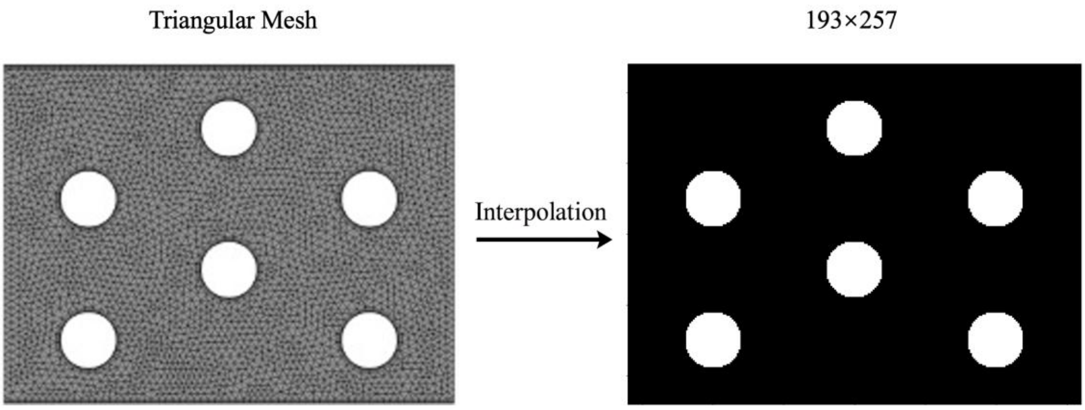

Figure 4 Interpolation from Triangular mesh to regular Cartesian grid.

An unstructured triangular mesh was employed for the CFD modeling, with local refinement applied around the cylindrical heat sources.

Under a representative operating condition, six levels of element sizes were tested (as shown in Figure 5), and the temperature distribution along the right boundary line was used as the convergence criterion.

When the element size was smaller than 1.0 mm, the temperature deviation converged to within 1%.

Meanwhile, the relative variations of the domain-averaged temperature and pressure drop were controlled within 1–2%, and the residuals of the continuity, momentum, and energy equations decreased below 10^{-5}, 10^{-5}, and 10^{-6}, respectively, indicating good numerical convergence of the steady-state solution.

Therefore, a mesh size of 1 mm (approximately 5×10^5 cells) was selected as the standard grid, achieving a balance between computational accuracy and cost.

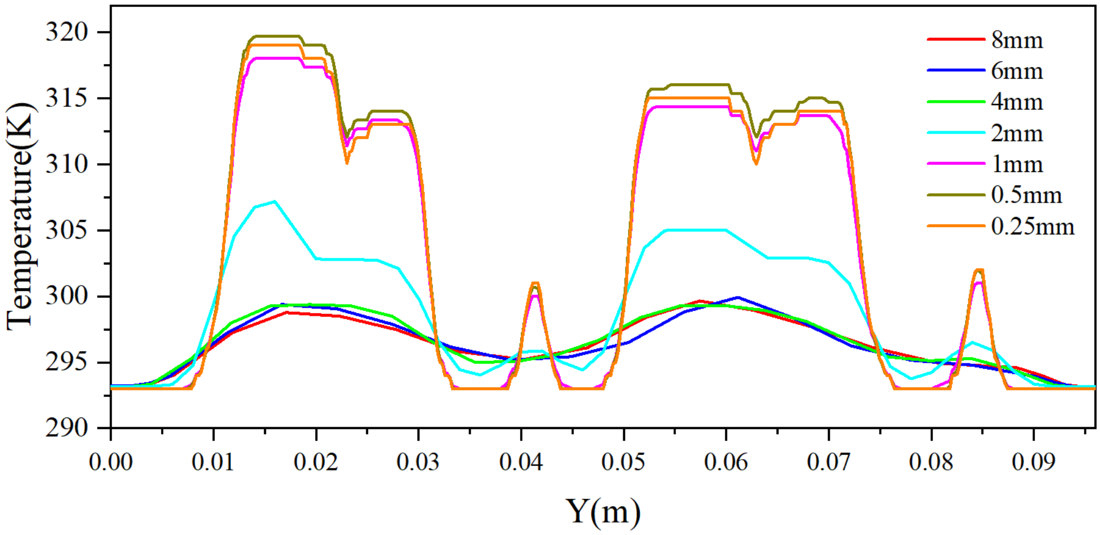

Figure 5 Grid Independence Test under a Representative Operating Condition.

To further validate the CFD dataset, we performed simulations using the k–ω standard and SST k–ω turbulence models under the same conditions. The comparison results show that the temperature fields predicted by all three models (laminar, k–ω standard, and SST k–ω) are highly consistent, with temperature differences within 0.1–0.5%. This confirms that the flow remains laminar under the present conditions, and the turbulence models have negligible impact on the results.

The present study intentionally focuses on a simulation–algorithm framework to establish a reliable and reproducible benchmark before introducing experimental uncertainties. The CFD datasets are derived from numerically validated models that ensure physical consistency, including mesh-independence verification, residual convergence, and realistic boundary conditions. These high-fidelity numerical data serve as a controlled environment to evaluate model performance, generalization, and robustness under varying sensor sparsity and geometric perturbations.

Importantly, the current simulation-based workflow represents the first stage of a broader digital-twin pipeline. Once the algorithmic framework and data-driven–physics-integrated methodology are consolidated, the approach will be transferred to real engineering systems through experimental data assimilation and sensor-based digital-twin updating. In this way, the validated CFD data not only provide a physically trustworthy training foundation but also act as a bridge connecting purely numerical studies to practical applications in industrial thermal–fluid monitoring and optimization.

4. Method

4.1 Framework Architecture of PISA-Net

This section introduces the details of the proposed Physics-Informed Structure-Aware Network (PISA-Net), a hybrid deep learning framework designed for reconstructing full-field temperature and velocity distributions in liquid cooling systems from sparse sensor data. As illustrated in Figure 6, PISA-Net consists of three key components: a sparse measurement encoder, a structure-aware decoder, and a hybrid loss function that incorporates both data supervision and physical constraints.

1) Sensor MLP Encoder: This module encodes the sparse measurement information from sensor points, including temperature, velocity, and spatial coordinates, using a multilayer perceptron (MLP). The encoded features are then projected into a high-dimensional latent space to capture local spatial-physical relationships.

2) U-Net Based Decoder: The encoded sensor features are concatenated with the binary mask matrix representing the fluid-solid domain geometry. These are then decoded through a U-Net architecture that progressively upsamples and reconstructs the spatially continuous fields, while preserving structural priors.

3) Physics & Data-Driven: The total loss function combines a data consistency loss, which enforces agreement with observed sensor values, and a physics-informed loss, derived from the steady-state energy equation. The joint optimization improves both prediction accuracy and physical consistency.

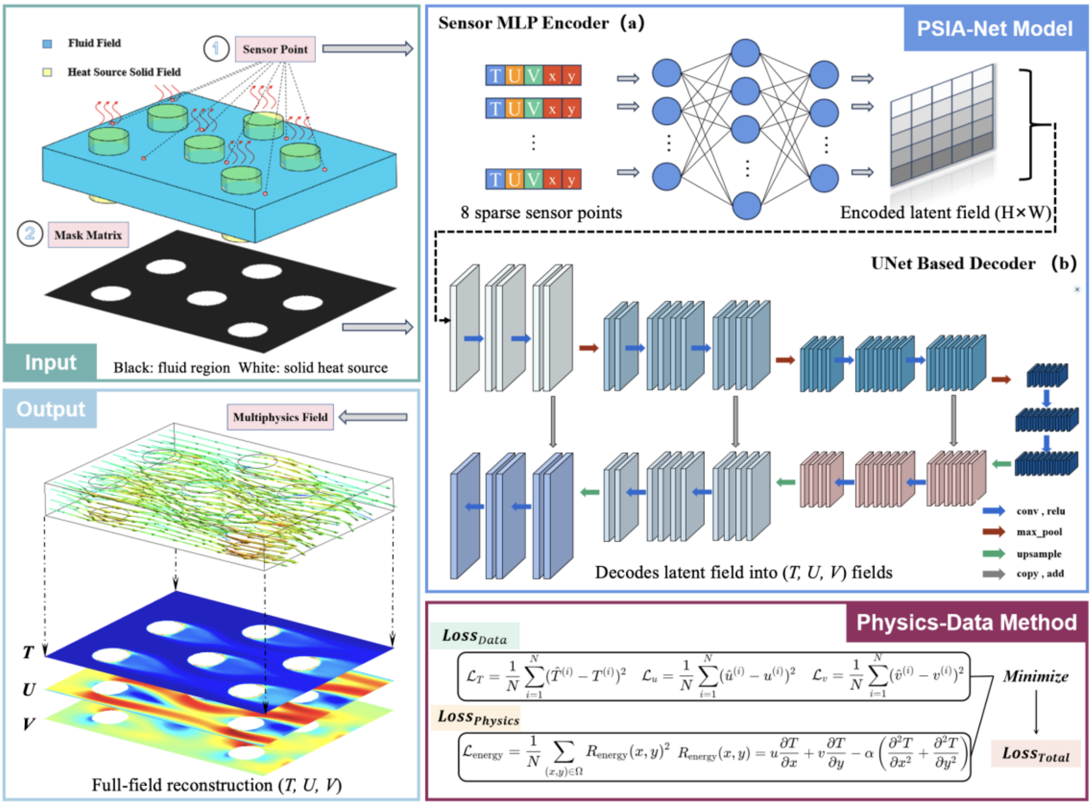

Figure 6. Overall Architecture of the Proposed PISA-Net Framework. (a) MLP Based Encoder for Sparse Sensor Data; (b)Structure-aware U-Net Based Decoder.

PISA-Net mainly consists of the following two sub-modules:

1) **Sparse Sensor Encoder**

As shown in Figure 7, The input of the model is composed of $N_s = 8$ sparse measurement points located at preset key positions. Each measurement point contains a five-dimensional feature vector to characterize its local state and spatial position information:

$$[T_i, u_i, v_i, x_i^{norm}, y_i^{norm}] \quad (6)$$

where, T_i, u_i, v_i are the observed values of temperature and velocity respectively, and (x_i^{norm}, y_i^{norm}) are the normalized coordinate positions. These measurement point data form the input tensor $\mathcal{D}_s \in \mathbb{R}^{N_s \times 5}$.

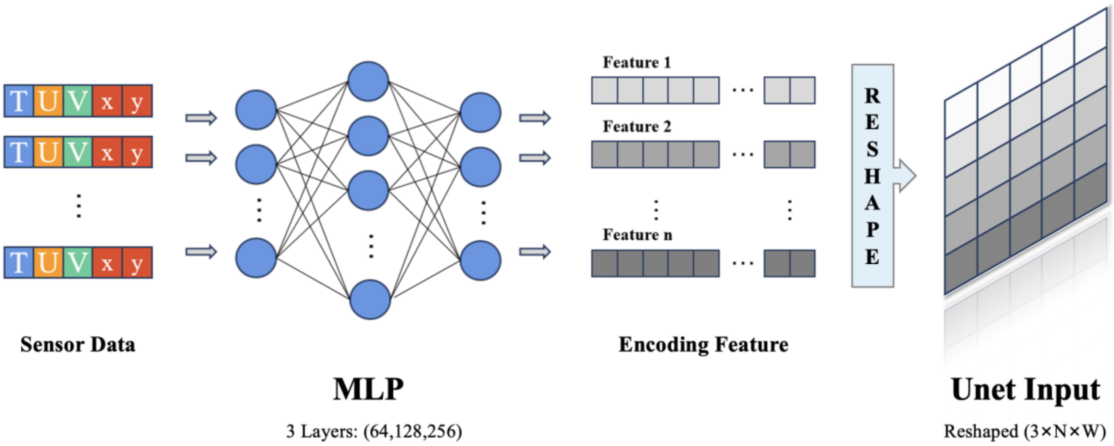

Figure 7. Sparse Sensor Encoder

The input tensor $\mathcal{D}_s$ is first mapped to local feature representations $f_i \in \mathbb{R}^d$ of the same dimension through a Multi-Layer Perceptron (MLP) encoder, and then all point features are concatenated into a global feature representation:

$$f_{global} = \mathrm{Concat}(f_1, f_2, \dots, f_8) \tag{7}$$

Subsequently, this one-dimensional feature is mapped to a medium-resolution initial feature map $C \times H' \times W'$ ($\mathbb{R}^{3\times48\times64}$) through a fully connected layer, and then upsampled to $C \times H \times W$ ($\mathbb{R}^{3\times193\times257}$) as the "initial guess" x_{init} input for field reconstruction.

2) **Structure -aware U-Net Decoder**

To enhance the model's ability to recognize structural boundaries and avoid unphysical predictions within the cylindrical heat source regions, a structure mask map $\mathcal{M}(x, y)$ is introduced, where a value of 1 denotes the fluid region and 0 denotes the solid heat source region, as shown in Figure 8. As a form of spatial prior, the mask explicitly encodes the geometry of non-flow domains, effectively constraining the network to perform feature extraction and prediction only within physically valid regions. This improves both the physical consistency and numerical stability of the model, especially near interfaces.

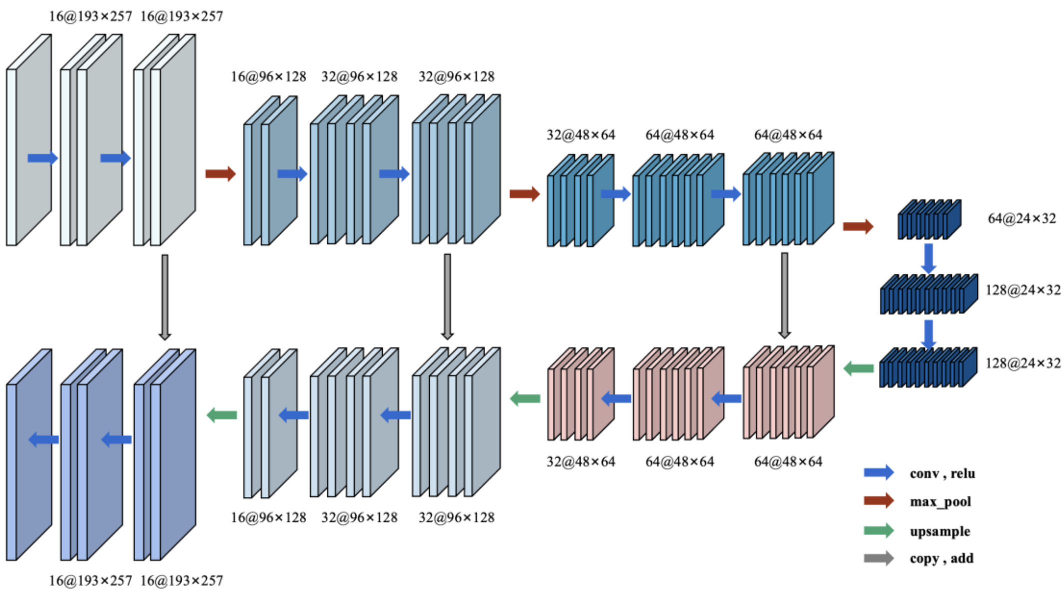

Figure 8. Structure-aware U-Net Decoder

In addition, this mechanism enables the network to generalize across varying heat source configurations. By replacing the structure mask input, the model can perform multiphysics field reconstruction for different structural layouts without modifying the network architecture or spatial discretization. This greatly enhances the generalization capacity and deployment flexibility of PISA-Net in cross-structural scenarios. Details on the construction of the structure mask and its role in enabling cross-structural adaptability are provided in Section 4.2.

The mask map is concatenated with the sparse encoding output along the channel dimension:

$$x_{input} = \mathrm{Concat}(x_{init}, \mathcal{M}) \tag{8}$$

Subsequently, the encoded sparse features are passed into the U-Net-based decoder for multi-scale reconstruction of the target physical fields. The architecture consists of three levels of downsampling and upsampling paths, with each stage composed of stacked convolutional modules. Each module contains two consecutive 3×3 convolution layers, followed by Group Normalization and ReLU activation, which are used to extract local spatial features and stabilize the training process.

Leveraging the skip connection mechanism inherent to the U-Net architecture, shallow structural features captured during downsampling are directly propagated to the corresponding upsampling stages. This effectively preserves fine-grained boundary details, particularly around the heat source regions. Simultaneously, deeper layers aggregate global multi-scale features, enhancing the network's ability to model the broader spatial distribution of the thermal–fluid fields.

Through this hierarchical architecture, the network achieves a balance between local feature alignment and global field reconstruction. This makes it well-suited for high-fidelity multiphysics field prediction tasks in geometrically complex domains

Finally, an end-to-end mapping neural network framework PISA-Net is constructed, which maps the input sparse measurement points $\mathcal{D}_s$ and structural mask $\mathcal{M}$ to the output multi-physics fields:

$$\mathcal{F}_\theta(\mathcal{D}_s, \mathcal{M}) \rightarrow \left[\hat{T}(x, y), \hat{u}(x, y), \hat{v}(x, y)\right] \tag{9}$$

where $\mathcal{F}_\theta$ represents the parameterized neural network model, i.e., PISA-Net. The specific parameters of the model can be found in the appendix.

4.2 Dynamic Structure Mask for Cross-Structural Generalization

The traditional methods suffer from a strong dependence on fixed geometric structures and exhibit poor generalization capability, often leading to significant degradation in reconstruction accuracy of temperature and velocity fields under varying geometric radii of embedded heat sources. To overcome these limitations, this study proposes a structure-aware neural network framework that incorporates a structure mask (Structure Mask) to explicitly encode geometric features and enable cross-structural transfer. By leveraging this design, the framework demonstrates robust generalization across diverse heat source geometries, achieving high-fidelity multiphysics field reconstruction even in the presence of structural perturbations.

Such capability highlights the method's superior adaptability to geometric variability and enhances its spatial generalization performance, which is critical for practical engineering deployment. To support this, PISA-Net incorporates a structure mask as an explicit geometric input. This mask encodes the spatial layout of the fluid–solid domain, allowing the model to operate within a unified input space and generalize across different heat source configurations without modifying the network architecture or retraining.

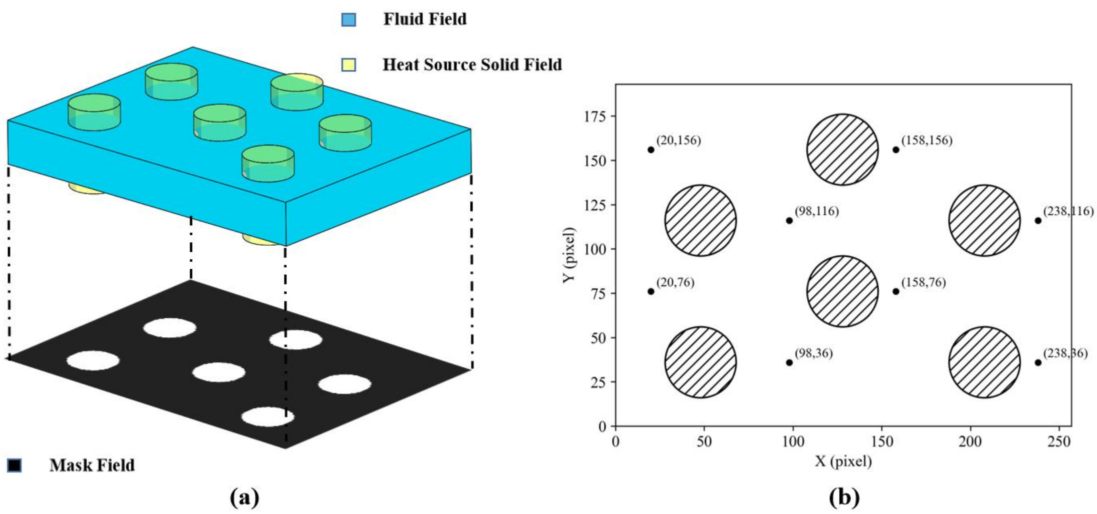

Figure 9. Schematic of Structural Mask Generation and Representation

Figure 9 illustrates the structural mask mechanism and its adaptability to different heat source radii:

1) Depicts the strategy for generating structural masks based on the center coordinates and radius of cylindrical heat sources;

2) Shows the resulting binary mask map $\mathcal{M}(x, y)$, where a value of 1 denotes the fluid region and 0 denotes the solid (cylindrical) region.

This pre-generation strategy enables the rapid construction of structure-aware masks without the need for remeshing, allowing the model to dynamically adapt to structural variations across different samples.

Notably, this design allows the model to perform field reconstruction even for unseen structural configurations during inference. By simply replacing the corresponding mask $\mathcal{M}(x, y)$, the network can generalize to new geometries without additional training or structural modifications. This significantly improves the model's flexibility and deployment efficiency in practical applications.

Overall, PISA-Net demonstrates strong cross-structural transferability, making it a promising tool for rapid thermal–fluid analysis and sensitivity studies in complex liquid cooling systems.

4.3 Physics-Embedded Constraint Formulation via Finite Difference Operators

This study proposes a novel method to address the challenge of reconstructing physical fields from highly sparse observations. The scarcity of ground-truth data hinders purely data-driven models from accurate reconstruction, while the lack of explicit physical constraints limits generalization under structural perturbations or changing operational conditions. Consequently, models often overfit to observed points and fail to respect the underlying governing equations, reducing the physical reliability of predictions.

To address these issues, this study incorporates physics-informed constraints into the data-driven framework by embedding the steady-state energy conservation law (i.e., the convection–diffusion equation) as a weakly supervised guidance signal. Specifically, the residuals of the governing equation are discretized using finite difference operators and introduced as an additional loss component during training. This strategy facilitates physical guidance under sparse supervision and enhances both the reconstruction accuracy and physical interpretability of the model. This component corresponds to the third module of the overall framework, as depicted in Figure 6(c).

The total loss function comprises two components: a data fidelity term and a physics-informed residual term. The detailed structure of the loss formulation is illustrated in Figure 10.

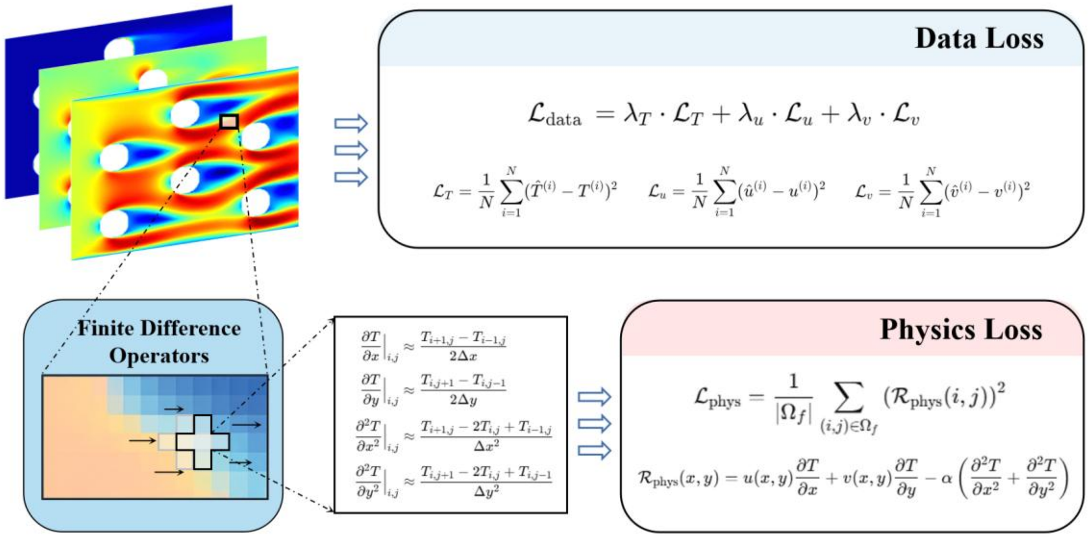

Figure 10. Data and Physics Hybrid-driven Strategy

Data Loss: Considering the limited sensor deployment within the liquid cooling system, supervised learning is applied exclusively at locations identified as fluid regions in the structural mask. Loss computations in solid regions—such as cylindrical heat sources—are excluded from the loss evaluation.

The specific definition of data loss is as follows:

$$\mathcal{L}_{\text{data}} = \frac{1}{\sum_{i,j} \mathcal{M}_{i,j}} \sum_{i,j} \mathcal{M}_{i,j} \cdot \left[(T_{i,j} - \hat{T}_{i,j})^2 + (u_{i,j} - \hat{u}_{i,j})^2 + (v_{i,j} - \hat{v}_{i,j})^2\right] \quad (10)$$

where $\mathcal{M}_{i,j} \in \{0,1\}$ represents the masked region, with 1 indicating the supervised region and 0 indicating the structural region. $\hat{T}, \hat{u}, \hat{v}$ are the output results, while T, u, v are the data-driven labels.

However, the supervision signals derived only from sparse observations are prone to causing violations of conservation laws, thus it is necessary to further introduce physical consistency constraints.

PDE Residual Loss (Physics-Informed Loss): To enhance physical consistency, this paper constructs an unsupervised residual loss based on the steady-state convection-diffusion equation. The output tensor is $\hat{Y} \in \mathbb{R}^{3\times H\times W}$, corresponding to the reconstructed temperature field $\hat{T}$, the horizontal component of the velocity field $\hat{u}$, and the vertical component $\hat{v}$ respectively. Suppose the output grid size is $H \times W$, the grid step sizes are Δx and Δy, and the corresponding pixel indices are $i = 1, \ldots, H, j = 1, \ldots, W$.

For each grid point $i = 1, \ldots, H, j = 1, \ldots, W$, the three channels in the model output tensor can be expressed as:

$$
\begin{aligned}
T_{i,j} &= \widehat{\mathbf{Y}}_{0,i,j} \\
u_{i,j} &= \widehat{\mathbf{Y}}_{1,i,j} \\
v_{i,j} &= \widehat{\mathbf{Y}}_{2,i,j}
\end{aligned}
\tag{11}
$$

To calculate the residual $\mathcal{R}_{\text{energy}}$ of the energy equation, we compute the first-order and second-order derivatives of the aforementioned output variables based on the two-dimensional central difference scheme.

First-order derivative:

$$
\begin{aligned}
\left(\frac{\partial T}{\partial x}\right)_{i,j} &\approx \frac{T_{i,j+1} - T_{i,j-1}}{2\Delta x} \left(\frac{\partial u}{\partial x}\right)_{i,j} \approx \frac{u_{i,j+1} - u_{i,j-1}}{2\Delta x} \\
\left(\frac{\partial T}{\partial y}\right)_{i,j} &\approx \frac{T_{i+1,j} - T_{i-1,j}}{2\Delta y} \left(\frac{\partial v}{\partial y}\right)_{i,j} \approx \frac{v_{i+1,j} - v_{i-1,j}}{2\Delta y}
\end{aligned}
\tag{12}
$$

Second-order derivative:

$$
\begin{aligned}
\left(\frac{\partial^2 T}{\partial x^2}\right)_{i,j} &\approx \frac{T_{i,j+1} - 2T_{i,j} + T_{i,j-1}}{\Delta x^2} \\
\left(\frac{\partial^2 T}{\partial y^2}\right)_{i,j} &\approx \frac{T_{i+1,j} - 2T_{i,j} + T_{i-1,j}}{\Delta y^2}
\end{aligned}
\tag{13}
$$

Residual of the energy equation (steady-state convection-diffusion equation):

$$
\mathcal{R}_{\text{energy},i,j} = u_{i,j} \cdot \left(\frac{\partial T}{\partial x}\right)_{i,j} + v_{i,j} \cdot \left(\frac{\partial T}{\partial y}\right)_{i,j} - \alpha \left[\left(\frac{\partial^2 T}{\partial x^2}\right)_{i,j} + \left(\frac{\partial^2 T}{\partial y^2}\right)_{i,j} \right] \tag{14}
$$

Using the mask map $\mathcal{M}_{i,j} \in \{0,1\}$, the cylindrical flow-disturbing heat source regions are excluded, and the residuals are calculated only within the fluid regions:

$$
\mathcal{L}_{\text{PDE}} = \frac{1}{\sum_{i,j} \mathcal{M}_{i,j}} \sum_{i,j} \mathcal{M}_{i,j} \cdot \left(\mathcal{R}_{\text{energy},i,j}\right)^2 \tag{15}
$$

The physical loss guides the model output to tend to satisfy the energy condition, thereby improving its physical rationality and generalization ability.

At the domain boundaries, spatial derivatives required for the PDE residual loss are computed using reflection padding, which extends the interior field values beyond the edges in a mirrored manner. This approach allows central differences to be applied uniformly across the entire grid, including boundary-adjacent points, without introducing one-sided numerical bias. This treatment ensures consistent numerical stencils, smooth derivative transitions, and stable residual evaluation near boundaries.

Total Loss Function Design:

The training loss of PISA-Net is formulated as a weighted sum of the data supervision term and the physics residual term, which jointly guide the network to balance fidelity to labeled data and adherence to physical laws. To enhance training stability and generalization capability, a Progressive Physics-guided Training Strategy is employed (see Section 4.4 for details).

4.4 Progressive Physics-guided Training Strategy

This section details the training strategy of PISA-Net, covering data preprocessing, the overall training procedure, the physics-guided loss injection mechanism, and the configuration of training hyperparameters.

Each training sample comprises three components:

1) Sparse Input Features: Measurements from eight fixed sensor locations, each providing five-dimensional input data, including temperature (*T*), horizontal and vertical velocities (*u, v*), and their corresponding spatial coordinates (*x, y*);

2) Structural Mask Map (Mask): A binary matrix of size 193×257 automatically generated based on the geometric position and radius of each cylindrical heat source. The fluid region is labeled as 1, while the solid heat source region is labeled as 0. This serves as prior geometric information to guide the network in focusing on physically valid domains;

3) Full-Field Ground Truth Labels: The complete temperature field T and velocity fields u and v, each with a resolution of 193×257, used for supervised learning and unsupervised physics residual computation.

All variables are normalized to the [0, 1] interval using Min-Max scaling. After interpolation onto a uniform grid, the data are formatted into tensors compatible with the input requirements of the network.

The training loss of PISA-Net is a weighted combination of the data supervision term and the physical residual term:

$$\mathcal{L}_{\text{total}} = \lambda_0 \mathcal{L}_{\text{data}} + \lambda_1(t)\mathcal{L}_{\text{PDE}} \tag{16}$$

where λ_0 is the hyperparameter for weighting the data loss, which is used to regulate the network's attention to real labels and is set to 10 based on experience, and $\lambda_1(t) > 0$ is the hyperparameter for weighting the physical loss, which is used to regulate the network's attention to real labels and physical consistency. To improve training stability and generalization performance, we introduce a Progressive Physics-Injection strategy: in the early stage of training (e.g., the first 200 epochs), only the data supervision loss $\mathcal{L}_{\text{data}}$ is applied to enable the model to fully learn sparse label information and avoid underfitting caused by the dominance of physical terms in optimization. As training progresses, the weight of $\lambda_1(t)$ is gradually increased to introduce the physical residual loss $\mathcal{L}_{\text{PDE}}$, providing structure-aware constraint guidance to ensure that the reconstruction results maintain physical consistency even in unlabeled regions.The variation form of the weight $\lambda_1(t)$ can be a smooth function such as linear, exponential, or cosine annealing; to improve stability, the following cosine increment strategy is adopted in this study:

$$\lambda_1(t) = \begin{cases} 0 & ,t < t_0 \\ \lambda_0 \cdot \dfrac{1 - \cos\left(\pi \cdot \dfrac{t - t_0}{t_1 - t_0}\right)}{2} & ,t_0 \le t < t_1 \\ \lambda_0 & ,t \ge t_1 \end{cases} \tag{17}$$

Where, t_0 represents the epoch at which the physical term starts to be introduced (200 epochs), and t_1 represents the epoch at which the physical term is fully weighted (400 epochs). λ_1 is the final weight of the physical loss, which is empirically set to $\lambda_1 = 0.1$ and shows a good balancing effect in multi-structure reconstruction.

5. Results and Discussion

5.1 Training Process and Convergence Analysis

The proposed method is implemented using the PyTorch 2.7 framework and trained on a workstation equipped with an Intel Core i9-13900KF processor and an NVIDIA GeForce RTX 4090 GPU. The Adam optimizer is employed with an initial learning rate of 1×10^{-3}, which is adaptively adjusted using a cosine annealing scheduler to promote stable convergence. The training is conducted for a total of 500 epochs with a batch size of 32, where each batch corresponds to an independent structural condition. This design ensures that gradient updates are decoupled across different geometrical configurations, thereby enhancing the model's robustness to structural perturbations and improving its cross-structure generalization capability.

The computation of PDE residuals is based on a central difference scheme for spatial discretization, with reflective boundary padding applied to improve the numerical stability of edge derivative calculations. Both the physical residual and supervised loss terms are evaluated strictly within the fluid regions defined by the structural mask, thereby avoiding the backpropagation of physically meaningless gradients from non-fluid (solid) areas.

A total of 300 simulated samples are used, with 70% allocated for training and 30% for testing. As shown in Figure 11, after introducing the physical loss, the data loss remains stable while the physical residual term consistently decreases throughout training, demonstrating the effectiveness of the proposed physics-guided strategy and the controllability of the training process. All model architecture details, hyperparameter configurations, and training codes are provided in Appendix A to ensure reproducibility.

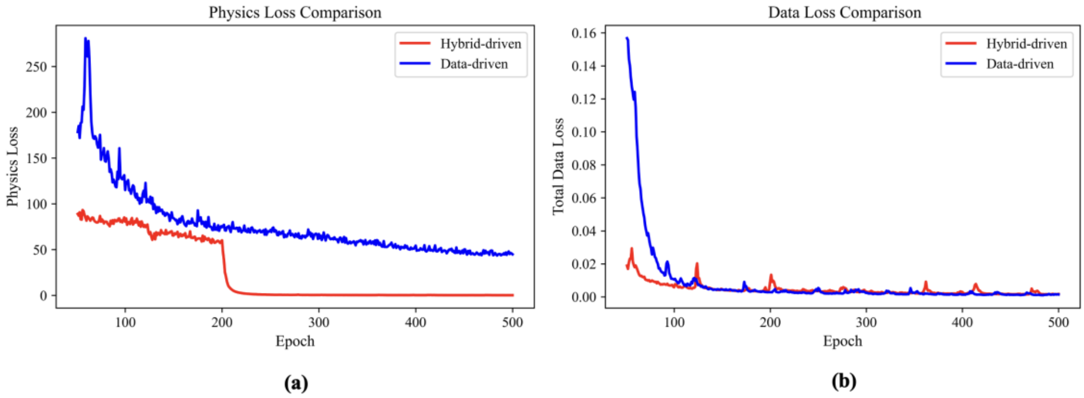

Figure 11. Physics and Data Loss Curves

5.2 Field Reconstruction Results under Varying Structures and Operating Conditions

To visually assess the multi-physics field reconstruction performance of the proposed structure-aware neural network, PISA-Net, several representative test samples are selected to showcase the reconstructed distributions of temperature (T), horizontal velocity (u), and vertical velocity (v). These results are further evaluated using quantitative error metrics.

Table 3 presents the reconstruction performance under various representative structural and operating conditions. The first column lists the corresponding input parameters for each condition, including inlet velocity, inlet temperature, heat flux, and heat source radius. The second column displays the reconstructed contour maps alongside the ground-truth distributions for qualitative comparison. The final two columns show the quantitative error metrics: normalized mean absolute error (NMAE) and root mean square error (RMSE), both computed within the structural mask region. The definitions of these metrics are provided in Section 5.3.

It is observed that PISA-Net consistently achieves accurate reconstructions across diverse structural and operational scenarios. The reconstructed temperature fields effectively capture the main channel gradients and heat diffusion patterns in disturbed flow regions. The horizontal velocity fields exhibit good continuity and directional coherence, while the vertical velocity fields maintain correct flow trends. The error metrics show that both NMAE and RMSE remain at low levels across all conditions. Moreover, the physical residual (PDE-R) distributions show no abnormal high deviations, indicating strong physical consistency in both supervised and unsupervised regions.

Overall, PISA-Net demonstrates stable and reliable reconstruction performance for temperature and velocity fields across varying structural configurations and working conditions.

Table 3. Display of Multiphysics Field Reconstruction Results

STATE	*T/u/v*	NMAE	RMSE
R= 10 T_{in}= 283.15 V_{in}= 0.03 Q=1.2×10^7	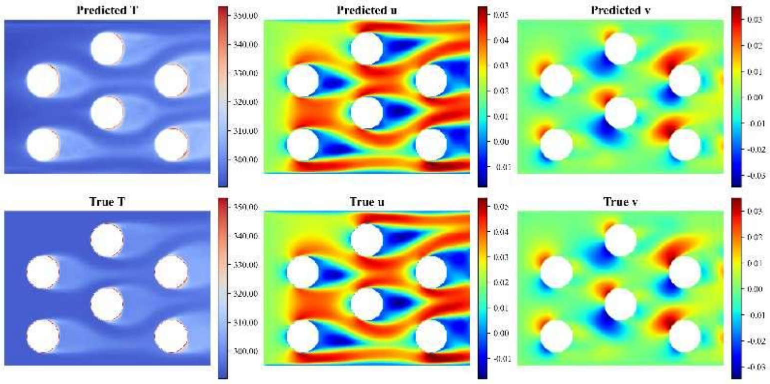	T=0.37 u=1.43 v=1.21	T=2.52 u=1.24 v=0.61
R= 6 T_{in}= 313.15 V_{in}= 0.02 Q=1.05×10^7	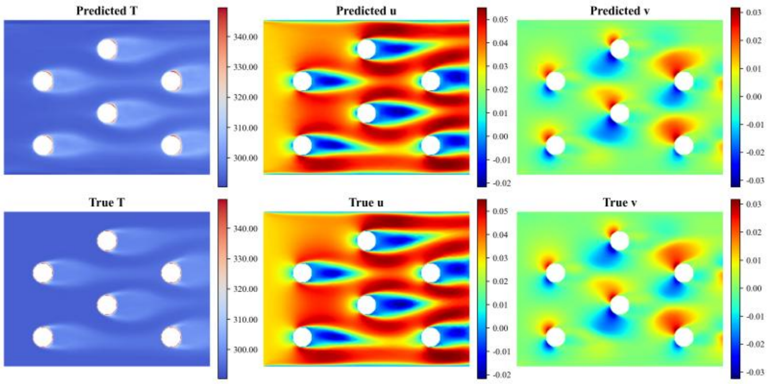	T=0.53 u=1.97 v=1.38	T=3.52 u=1.07 v=0.31
R= 8 T_{in}= 293.15 V_{in}= 0.05 Q=0.9×10^7	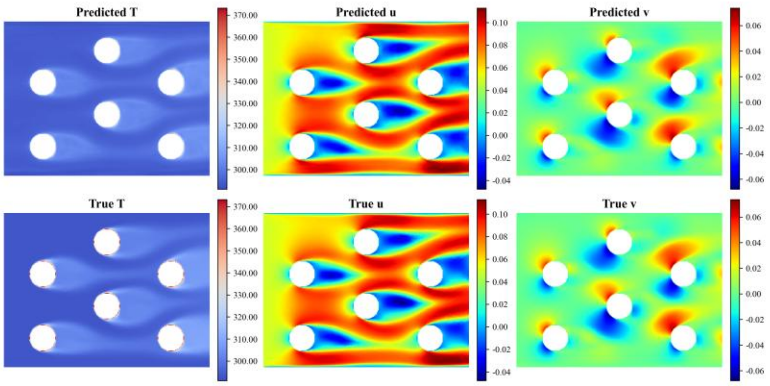	T=0.54 u=0.97 v=0.88	T=4.51 u=0.96 v=0.81

5.3 Evaluation of Multiphysics Field Reconstruction Performance

To quantitatively evaluate the multi-physical field reconstruction performance of the proposed PISA-Net framework, this paper employs two metrics, namely Normalized Mean Absolute Error (NMAE) and Root Mean Square Error (RMSE), to systematically assess the model's reconstruction results in three physical fields: temperature field (T), horizontal velocity (u), and vertical velocity (v).

The two types of error indicators are defined as follows:

$$\mathrm{NMAE} = \frac{1}{N}\sum_{i=1}^{N}\frac{|y_i - \hat{y}_i|}{y_{max} - y_{min}}$$

$$\mathrm{RMSE} = \sqrt{\frac{1}{N}\sum_{i=1}^{N}(y_i - \hat{y}_i)^2} \qquad (18)$$

Where y_i and $\hat{y}_i$ represent the true and reconstructed values within the masked region, respectively, and $\hat{y}_i$ is the number of effective sampling points.

Figure 12 and Figure 13 illustrate the model's performance on multiple structural working condition samples from the test set, the following observations can be made:

The error in the temperature field T is the smallest overall, indicating that in steady-state forced convection problems, temperature distributions are relatively smooth and easier to reconstruct from sparse points.

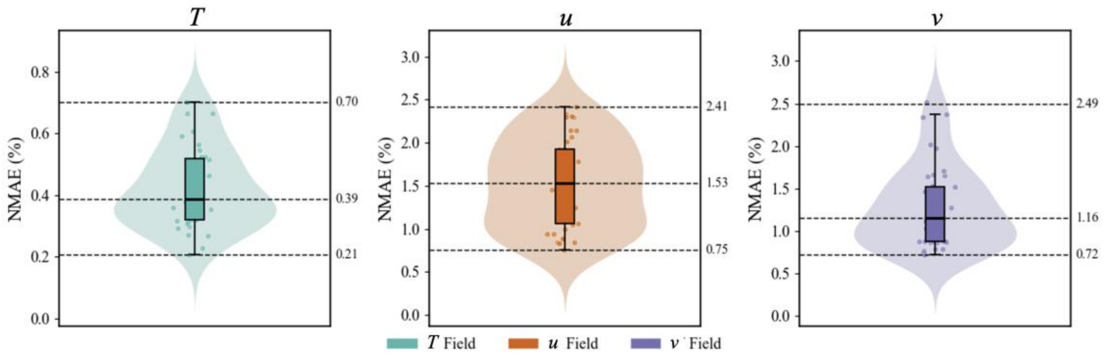

Figure 12 NMAE for *T*, *u*, and *v* Fields Reconstruction

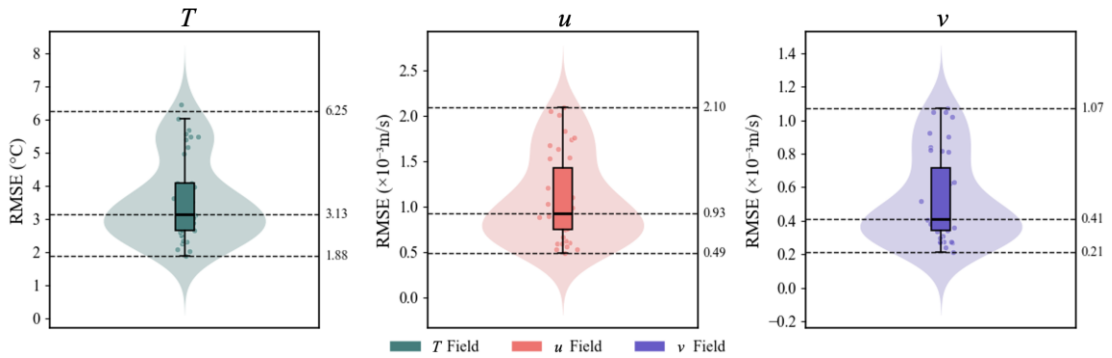

Figure 13. RMSE for *T*, *u*, and *v* Fields Reconstruction

The error in the horizontal velocity u is slightly higher, reflecting the uncertainty introduced by flow-direction disturbances in velocity reconstruction.

The error distribution for the vertical velocity v is the widest, being significantly influenced by strong gradients upstream/downstream of the heat source cylinders, where local disturbances are more pronounced.

The median errors for all three fields remain at low levels, demonstrating the network's robustness and generalization ability across various structural disturbances and boundary conditions.

Notably, outliers in the error distribution for some samples are primarily concentrated in regions with densely distributed heat source cylinders. These areas exhibit complex flow patterns due to enhanced local convection, posing ongoing challenges. Overall, PISA-Net consistently and accurately reconstructs temperature and velocity fields under varying cylinder configurations and heat source sizes, providing a solid foundation for subsequent thermal management optimization and structural diagnostics.

Figure 14 presents the contour maps of the local absolute error and RMS-normalized local error for the reconstructed temperature (T) and velocity components (U, V) under a representative working condition.

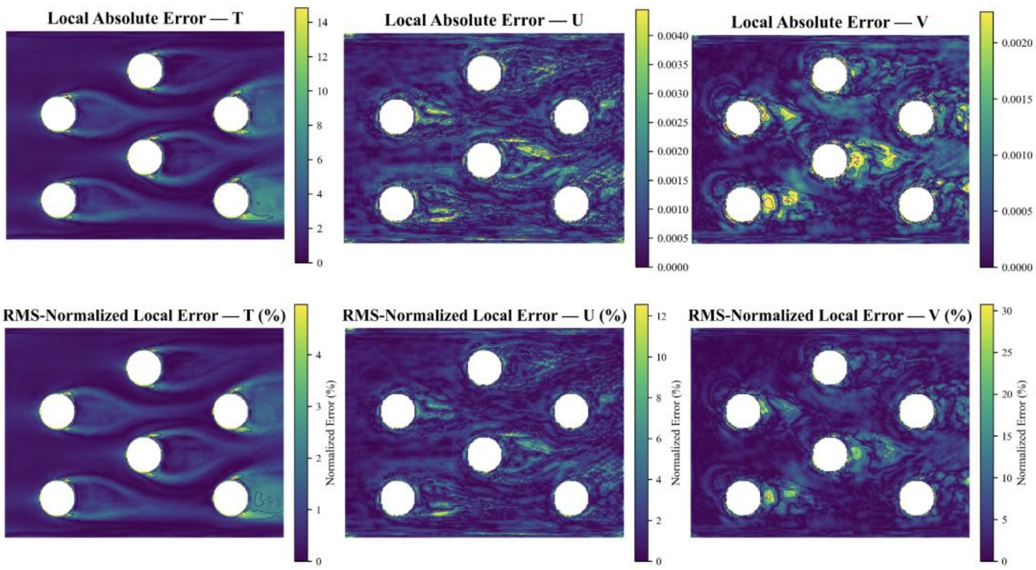

Figure 14. Contour maps of the local absolute error (top) and RMS-normalized local error (bottom) for the reconstructed temperature (T) and velocity components (U, V) under a representative working condition.

These two indicators together provide a comprehensive view of the spatial error patterns: the local absolute error quantifies the magnitude of pointwise deviations, while the RMS (Root Mean Square) -normalized error reveals the relative deviation with respect to the global energy scale of each physical field. Across all conditions, the hybrid-driven model exhibits excellent reconstruction performance.

$$\text{local absolute error} = |y_i - \hat{y}_i| \tag{19}$$

$$\text{RMS} - \text{normalized error} = \frac{|y_i - \hat{y}_i|}{\sqrt{\frac{1}{N}\sum_{i=1}^{N} {y_i}^2}}$$

The local absolute error maps show that the majority of the temperature deviations remain below 2 K, and velocity deviations are within 0.004 m s^{-1} in the mainstream regions. When normalized by the field RMS values, the RMS-normalized local errors are mostly confined within 1–3 % for *T*, *U*, and *V*, indicating highly consistent accuracy across variables with different magnitudes.

Notably, relatively larger normalized errors appear in two characteristic areas:

(1) Near the heat-source walls, where strong thermal gradients and intense heat transfer lead to mismatch in local wall-normal derivatives of *T*; and

(2) In the wake regions behind disturbance columns, where flow separation and recirculation produce highly nonlinear velocity fluctuations.

In these zones, the model slightly underpredicts local vortex-induced velocity variations, yet still maintains coherent global flow and thermal patterns.

Overall, the spatial distributions of both indicators demonstrate strong physical interpretability: the hybrid-driven model accurately captures the large-scale thermo-fluid behavior, confirming the model's robustness and physical consistency.

5.4 Ablation Study on the Effect of Physics-Informed Constraints

To further verify the role and necessity of physics-informed embedding in the multi-physical field reconstruction task, this paper designs an ablation experiment on the physical loss to investigate the performance changes of the model without introducing$\mathcal{L}_{\text{PDE}}$.

We train two versions of PISA-Net based on the same network structure and training process:

Data-Driven Model: Includes only the data supervision term$\mathcal{L}_{\text{data}}$without physical residual constraints.

Hybrid-Driven Model: Employs the full loss function$\mathcal{L}_{\text{total}} = \lambda_0\mathcal{L}_{\text{data}} + \lambda_1(t)\mathcal{L}_{\text{PDE}}$ (see Section 4.4 for details).

The experiments are conducted on the same test set. We record the PDE Residual and NMAE of both models across the three physical fields (T, u, v) and compare their error distributions and physical consistency.

Figure 15 shows a comparison between our method and the data-driven method. It is evident that after introducing physical information constraints, the smoothness and realism of the flow field and temperature field are more consistent with the real physical fields. In the following, we will conduct comparisons using various indicators and cloud images.

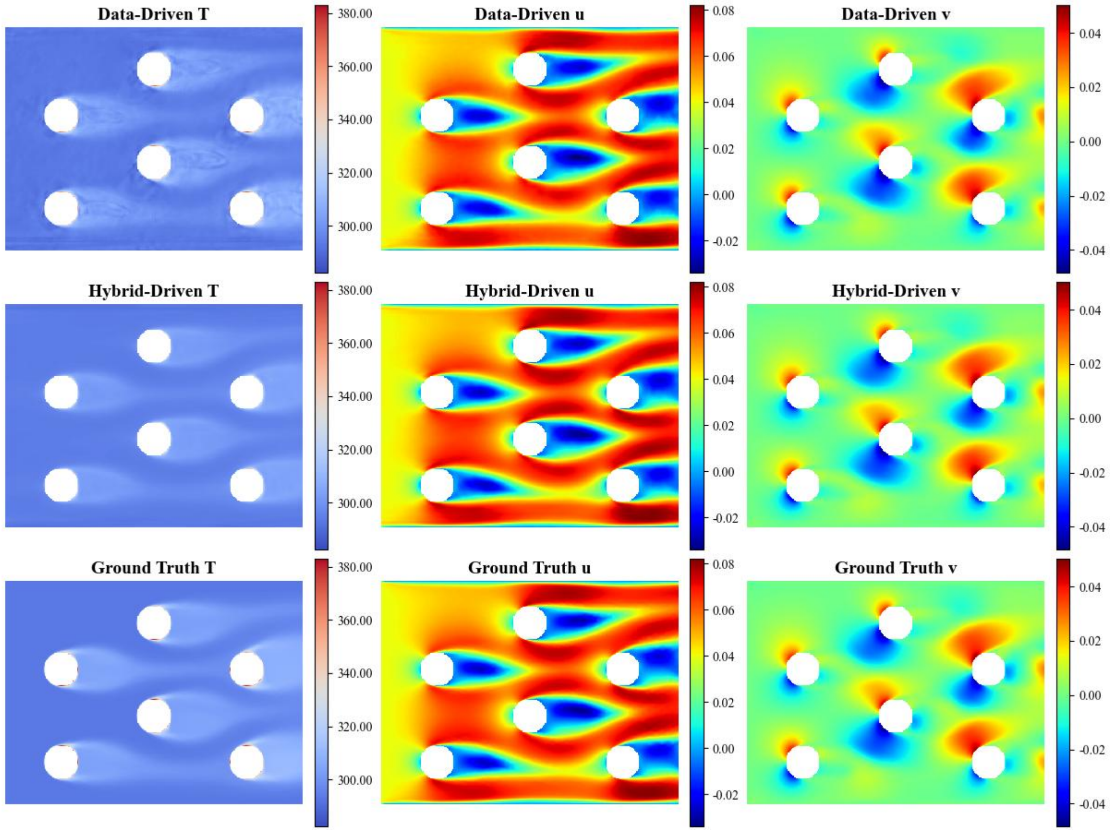

Figure 15. Comparison of Data-Driven and Hybrid-Driven Reconstructions Against Ground Truth for T, u, and v Fields

Figure 16(a) shows the NMAE error plots of the two models on the test set. It can be seen from the results that after introducing physical constraints, the overall errors of the temperature and velocity fields decrease, and the number of abnormal value is reduced, indicating that physics-informed embedding enhances the robustness of the model. Figure 16(b) presents the PDE Residual error plots of the two models on the test set. The results reveal that with the introduction of physical constraints, the physical residuals decrease by multiples and the number of outliers is reduced, demonstrating that physics-informed embedding significantly improves the physical interpretability of the model.

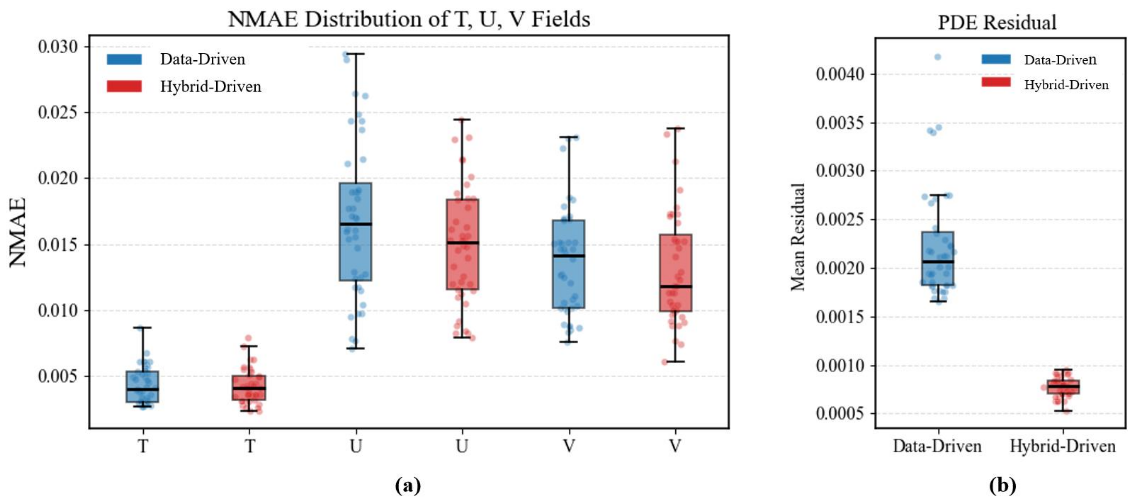

Figure 16. Error Evaluation of the Two Types of Models on the Test Set

Although the hybrid-driven reconstructions in Figure 15 generally exhibit closer agreement with the ground truth across most regions, the data-driven results appear slightly more similar near the heat-source sides. This difference does not arise from interpolation but from the distinct optimization objectives of the two models. Both were evaluated on the same Cartesian grid, ensuring consistent spatial resolution. The data-driven model focuses solely on minimizing pixel-wise MSE, which emphasizes local similarity, while the hybrid-driven model jointly minimizes data and physics-based residual losses, preserving thermal fluid coupling and enforcing conservation consistency. As a result, the hybrid-driven model maintains physically accurate gradients that may appear slightly vague but represent more realistic flow behavior. The improved quantitative metrics in Figure 16 further confirm its higher physical fidelity and numerical accuracy.

As shown in Figure 17, by comparing the physical fields reconstructed by the two methods, it can be found that our reconstruction method solves the problems of physical field discontinuity and gradient anomalies caused by the pure data-driven method. Specifically, such anomalies manifest as ripples and checkerboard patterns in the fields, which are all caused by the fact that the pure data-driven method does not take physical information into account.

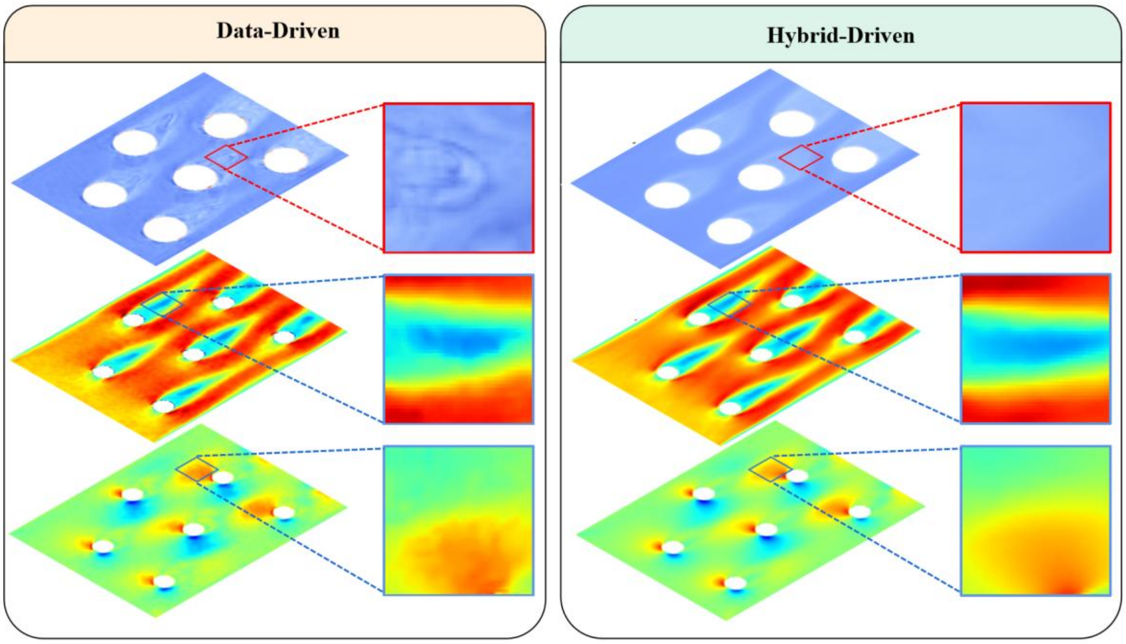

Figure 17. Detailed Comparison of Physical Informed Effects

Meanwhile, Figure 18 shows the heat map of the residual distribution R_{energy} of the energy equation under a typical flow-disturbing condition. The model without introducing physical terms exhibits large residual values in the vicinity of and downstream from the flow-disturbing cylinders, showing obvious physical inconsistency; whereas after introducing $\mathcal{L}_{\text{PDE}}$, the residual values converge overall, and in particular, better smoothness and conservation are demonstrated in the boundary transition regions.

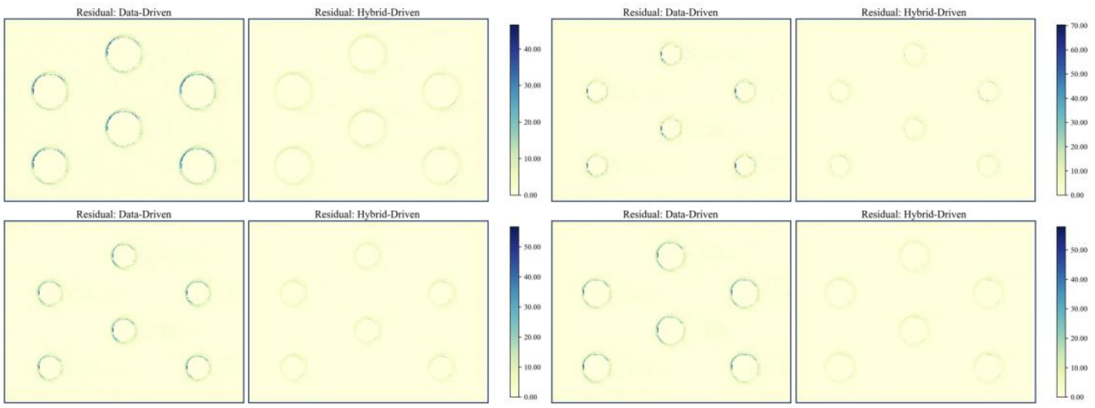

Figure 18. Distribution Map of Physical Residuals

In summary, physics-informed can not only effectively compensate for the lack of supervision caused by sparse data, but also significantly improve the physical consistency of the model in disturbed regions and downstream regions, providing important support for achieving interpretable and generalizable multi-physical field reconstruction.

5.5 Comparative Study of Network Structures with Baseline Models

To systematically assess the capability of the proposed structure-aware decoder in reconstructing multi-physics fields, this section conducts comparative experiments with baseline decoder architectures. Two representative convolutional decoding structures are selected: (i) a ResNet-34 decoder incorporating deep residual connections, and (ii) a standard convolutional network without skip connections, referred to as Baseline-CNN. All three models (including the proposed U-Net decoder in PISA-Net) share identical input configurations, network capacity, and training strategies. Each takes as input sparse physical observations and structural masks, and outputs full-field predictions of temperature and velocity distributions (T, u, v).

Table 4 presents the reconstruction error comparison of these decoders under typical test conditions, including the Normalized Mean Absolute Error (NMAE) for the three fields and the PDE-based physical consistency metric derived from the residual of the steady-state convection-diffusion equation. The results demonstrate that the U-Net decoder achieves the best performance across all metrics, with a temperature field NMAE of 3.12% and a PDE residual as low as 0.0007, significantly outperforming the ResNet-34 and Baseline-CNN structures.

In particular, although ResNet-34 benefits from residual connections that enhance deep feature stability, it suffers from blurred boundaries and noisy velocity reconstructions due to its limited capacity in multi-scale feature fusion and shallow detail preservation. On the other hand, the Baseline-CNN, despite its simplicity, lacks the ability to effectively capture turbulent structures and geometric boundary variations, leading to inferior accuracy and physical consistency. In contrast, the U-Net decoder's symmetric structure and skip connections facilitate efficient fusion of low-level spatial and high-level semantic features, enabling accurate recovery of fine-scale boundary details and consistent full-field reconstructions.

In summary, the proposed structure-aware decoder in PISA-Net demonstrates superior generalization capability and robustness across diverse structural and operational scenarios, offering an effective solution for sparse-sensor-based thermal–fluid field reconstruction.

Table 4. Comparison of Reconstruction Errors Under Different Decoder

Structure	NMAE (T)	NMAE (u)	NMAE (v)	PDE Residual ($T/u/v$)
U-Net	3.12	3.44	3.01	0.0007
ResNet-34	4.45	4.89	4.12	0.0014
Baseline-CNN	4.83	4.92	4.45	0.0016

Beyond reconstruction accuracy, we also analyzed the computational performance and methodological positioning of PISA-Net relative to other modeling paradigms. Once trained, PISA-Net reconstructs full temperature and velocity fields from sparse-sensor inputs within milliseconds, whereas a single CFD forward simulation typically requires several minutes even on parallel hardware. This computational efficiency makes PISA-Net promising for real-time monitoring and digital-twin updating in industrial cooling systems where boundary conditions are partially unknown and sensor coverage is sparse.

The present study tackles an inverse field-reconstruction problem (sparse → full field) rather than a conventional forward prediction. Operator-learning frameworks such as the Fourier Neural Operator (FNO) and Deep Operator Network (DeepONet) assume dense inputs and fixed mesh topology, and thus cannot directly handle sparse-sensor, geometry-varying scenarios without major architectural redesigns. Bayesian inversion methods, although effective for uncertainty quantification, require repeated PDE solves or large-scale sampling, which is computationally prohibitive for complex thermo-fluid systems.

PISA-Net is specifically designed for such sparse-sensor, multi-geometry inverse problems. It integrates a sparse-sensor encoder, structure-aware mask input, and lightweight PDE regularization to achieve physically consistent reconstructions. Unlike classical Physics-Informed Neural Networks (PINNs), which use PDE residuals as the main optimization objective and often converge slowly, PISA-Net treats physics-based residuals as auxiliary constraints that guide supervised learning toward physically meaningful solutions. Classical PINNs are suited for forward or inverse PDE solving with fully known boundary and initial conditions. However, when applied to inverse problems where boundary information is unknown and only sparse sensor data are available, PINNs become highly inefficient—requiring exponentially more collocation points and days of training due to the lack of data-driven guidance.

In contrast, PISA-Net efficiently combines limited sensor data with physics-based residuals computed within the fluid domain, enabling convergence within hours while maintaining physical consistency. From a probabilistic viewpoint, the physics residuals encode prior knowledge of admissible field behavior, whereas the supervised term enforces agreement with sensor observations. Embedding both into a unified loss function ensures data fidelity and physical realism without costly posterior sampling.

Overall, PISA-Net bridges data-driven inference and physics-based modeling, providing two key advantages over existing forward-learning frameworks: (1) robust reconstruction from highly sparse and irregular sensor inputs, and (2) strong cross-geometry generalization without retraining. These properties make it a practical solution for large-scale, sparse-sensor inverse field reconstruction in engineering applications.

5.6 Impact of Sensor Configuration on Reconstruction Performance

To further assess the reconstruction capability of the proposed PISA-Net under sparse observation conditions and investigate the influence of sensor deployment density on reconstruction performance, a series of controlled experiments are conducted with varying sensor quantities and layouts. Specifically, under fixed structural and boundary condition parameters, each sample is configured with 4, 6, 8, 10, 12, and 14 measurement points, respectively. The temperature and velocity information at these locations is extracted as model input, while the reconstruction results of the three physical fields (*T, u, v*) serve as output. All sensors are positioned within the fluid region, with their locations selected based on a combination of uniform grid sampling and engineering feasibility.

The sensor positions were deliberately selected according to the flow and thermal characteristics of the cooling plate. The layout follows the geometric symmetry of the domain and aims to capture the dominant spatial gradients of temperature and velocity. Specifically, sensors were placed in three representative regions: (1) the inlet and central channel to reflect the global inflow condition and main flow direction; (2) the cylinder-side shear layers where the velocity and temperature gradients are strongest; and (3) the wake region that contains the major recirculation and convective mixing effects. As the number of sensors increases (from 4 to 14), the placement progressively extends from these dominant zones toward the peripheral regions, enhancing coverage of the flow domain. This symmetric and feature-oriented configuration ensures that a small number of sensors can effectively represent the main physical variations of the system.

To quantify reconstruction accuracy, the Normalized Mean Absolute Error (NMAE), as defined in Section 5.2, is adopted as the primary evaluation metric across different sensor configurations.

The experimental results are illustrated in Figure 19. As the number of sensors increases, the reconstruction error exhibits a pronounced decreasing trend. Notably, when the number of sensors increases from 4 to 8, the NMAE shows the most substantial drop, indicating that a moderate increase in observational information significantly enhances the model's spatial representation capability. However, when the number of sensors exceeds 10, the performance gain becomes marginal, demonstrating an "information saturation" effect. This suggests that PISA-Net already achieves high reconstruction accuracy under moderate observation densities, and further increasing sensor counts yields diminishing returns.

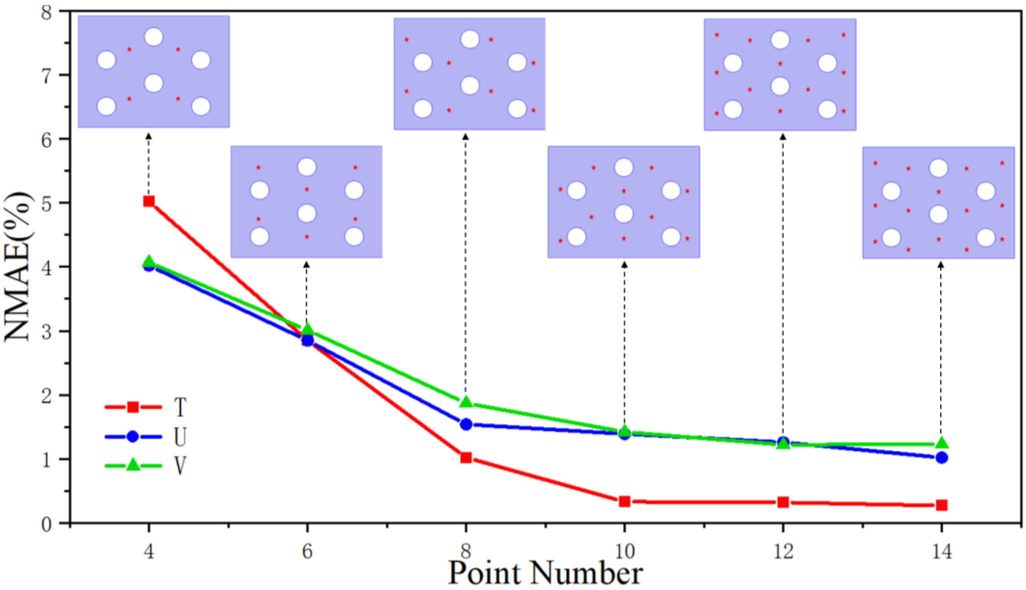

Figure 19. The Influence of the Number and Layout of Sensors on Accuracy

It is worth noting that even under the extremely sparse input condition with only 6 sensors, PISA-Net can still control the error within an acceptable range. This result demonstrates the inherent generalization ability and physical consistency guiding effect of the model after integrating the structure mask and physical residual mechanism.

In summary, the experiments in this section verify that PISA-Net still has good robustness and generalization ability under low-observation conditions, and optimal performance can be achieved when the number of sensors is 8 or more.

6. Conclusion

To tackle the multi-physical field reconstruction problem in liquid cooling systems from sparse sensor deployment, variable heat source geometries, and diverse operating conditions—this study proposes a deep learning framework that integrates structure-awareness and physics-based constraints: PISA-Net (Physics-Informed Structure-Aware Network). By leveraging limited temperature and velocity measurements, together with a geometry-guided structural mask and a physics-informed loss function derived from the energy conservation equation, the proposed method achieves high-fidelity reconstruction of steady-state thermal–flow fields across varying structural scales and working conditions. The model demonstrates superior generalization across geometries and enhanced physical consistency. The core contributions of this work are as follows:

1) Sparse-observation-driven multi-physics field reconstruction – A nonlinear mapping is established from sparse temperature and velocity measurements to full-field physical distributions, significantly reducing sensor density and measurement costs while

maintaining suitability for engineering deployment.

2) Geometric awareness fundamentally enhances cross-structural adaptability – Incorporating structure masks enables the model to perceive and adapt to variations in embedded heat source geometries, maintaining stable accuracy across unseen structural configurations.

3) Embedding physics laws improves both fidelity and interpretability – A physics-informed loss based on the energy conservation equation substantially reduces residual deviations, especially in regions of strong flow disturbance, and provides physically consistent reconstructions under sparse supervision.

In summary, the proposed framework offers an effective and scalable solution to the inverse reconstruction problem in liquid cooling systems. It holds substantial theoretical value and application potential in intelligent thermal management, digital twin systems, thermal performance assessment, and fault detection. In future work, we plan to extend the framework to higher Reynolds number regimes by incorporating turbulence models or higher-fidelity CFD data, thereby assessing its robustness under more complex flow conditions and broadening its applicability to a wider range of engineering scenarios.

Appendix A. Network architecture and training of PISA-Net

A.1. Overall framework

PISA-Net (Physics-Informed Structure-Aware Network) is designed for sparse-sensor inverse field reconstruction under multi-geometry cooling structures. It consists of two main sub-networks: (1) an MLP-based sparse-sensor encoder that embeds discrete measurements into a latent feature space, and (2) a structure-aware U-Net decoder that reconstructs full-field temperature and velocity distributions guided by both data supervision and PDE-based physical consistency.

A.2. Network architecture details

The overall network architecture includes both an MLP encoder and a structure-aware U-Net decoder. The details of each module are summarized in Tables A1–A3.

Table A1. Sparse-sensor encoder.

Layer	Input dimension	Output dimension	Activation	Description
MLP-1	5 (T, u, v, x, y)	64	ReLU	Encodes single-point measurement features
MLP-2	64	128	ReLU	Expands latent

				representation
MLP-3	128×Ns (Ns=8 sensors)	256	ReLU	Projects embedding to higher-dimensional latent space
Output Reshape	256	3 × H × W	—	Interpolated to regular grid and concatenated with structural mask

Table A2. Structure-aware U-Net decoder.

Block	Output shape	Kernel/stride	Activation	Normalization
Input	3 ×193 × 257	1×1 / 1	ReLU	—
Encoder-1	16 × 193 × 257	3×3 / 2	ReLU	GroupNorm
Encoder-2	32 × 96 × 128	3×3 / 2	ReLU	GroupNorm
Encoder-3	64 × 48 × 64	3×3 / 2	ReLU	GroupNorm
Bottleneck	128 × 24 × 32	3×3 / 1	ReLU	GroupNorm
Decoder-1	64 × 48 × 64	3×3 / 1	ReLU	GroupNorm
Decoder-2	32 × 96 × 128	3×3 / 1	ReLU	GroupNorm
Decoder-3	16 × 193 × 257	3×3 / 1	ReLU	GroupNorm
Output	3 ×193 × 257	1×1 / 1	—	—

Table A3. Model summary.

Sub-module	Parameters	Description
Sparse-sensor MLP encoder	~0.3 M	Encodes discrete measurements into latent space
Structure-aware U-Net decoder	~5.3 M	Performs full-field reconstruction with physics guidance
Total	≈ 5.6 M	Balanced model capacity and efficiency

A.3. Training configuration

Optimizer: Adam. Initial learning rate: 1×10^{-3}. Scheduler: Cosine annealing with warm restarts. Batch size: 32. Epochs: 500. Loss: $\mathcal{L}_{\text{total}} = \lambda_0\ \mathcal{L}_{\text{data}} + \lambda_1(t)\mathcal{L}_{\text{PDE}}$, where $\mathcal{L}_{\text{data}}$ is the MSE of (T, u, v) in the fluid domain, and $\mathcal{L}_{\text{PDE}}$ represents energy and mass residuals. The weight $\lambda_1(t)$ = 0.05 is activated after 200 epochs. Normalization: channel-wise min–max. Framework: PyTorch 2.7. Hardware: NVIDIA RTX 4090 GPU (24 GB), training time ≈ 1 hours.

A.4. Training procedure

Stage I (supervised pretraining): train for 200 epochs with $\mathcal{L}_{\text{data}}$ only. Stage II (hybrid fine-tuning): gradually activate $\mathcal{L}_{\text{PDE}}$ with λp=0.05 to balance data and physics. Gradient clipping (1.0) is applied to avoid instability. The cosine annealing scheduler reduces the learning rate to 1×10^{-5}.

A.5. Dataset and reproducibility

The dataset contains simulated flow and temperature fields under five structural configurations and multiple inlet conditions (300 samples total). Each sample includes full-field labels (T, u, v) and corresponding sparse-sensor inputs (8 measurement points). Both the dataset and source code will be released upon publication to promote reproducibility and community adoption. The corresponding code and documentation can be accessed via the author's GitHub repository:

GitHub URL: https://github.com/DDBLB/PISA-Net

This repository provides comprehensive guidance for reproducing the proposed PISA-Net framework, including dataset preprocessing, training scripts, and evaluation procedures.

Acknowledgments

This research was financially supported by the National Key R&D Program of China (2022YFF1400302), the National Natural Science Foundation of China (Grant No.12432005, No.12472116), These supports are gratefully acknowledged.

References

[1] Shi, G., Qin, F., Yang, G., & Dai, Y. (2024, August). Heat Dissipation Optimization Study of Active Phased Array Antenna Microchannel. In *2024 25th International Conference on Electronic Packaging Technology (ICEPT)* (pp. 1-4). IEEE.

[2] Liu, W., Xu, G., Gu, X., Yao, J., Li, M., Lei, M., ... & Fu, Y. (2025). Experimental analysis and thermodynamic modeling for multilevel heat exchange system with multifluid in aero engines. *Energy*, *315*, 134373.

[3] Zhao, X., Yin, J., Jiang, J., Lan, R., Wang, J., & Zhao, D. (2025). A review on thermal collection management and conversion performance enhancement of extended range electric vehicle exhaust thermoelectricity. *Applied Thermal Engineering*, 126476.

[4] Lee, J. H., & Kim, T. Y. (2025). Reconstruction of flow and temperature fields of exhaust gas flow for enhancing the energy harvesting performance of a thermoelectric generator. *Applied Thermal Engineering*, 128035.

[5] Zhan, S., Liang, L., Li, Z., Yu, C., & Wang, F. (2024). Topology optimization of liquid cooling plate for lithium battery heat dissipation based on a bionic leaf-vein structure. *International Journal of Heat and Mass Transfer, 231*.

[6] Zhu, Z., Zhang, Y., Chen, A., Chen, J., Wu, Y., Wang, X., & Fei, T. (2025). Review of integrated thermal management system research for battery electrical vehicles. *Journal of Energy Storage*, *106*, 114662.

[7] Yan, K., Liu, D., & Yan, J. (2024). Topology optimization method for transient heat conduction using the Lyapunov equation. *International Journal of Heat and Mass Transfer*, *231*, 125815.

[8] Zheng, R., Wu, Y., Li, Y., Wang, G., Ding, G., & Sun, Y. (2022). Development of a hierarchical microchannel heat sink with flow field reconstruction and low thermal resistance for high heat flux dissipation. *International Journal of Heat and Mass Transfer, 182*, 121925-.

[9] Sun, W., Li, P., Cheng, W., Li, C., Qi, X., Shen, H., & Shao, X. (2025). Novel hybrid thermal management system for cylindrical lithium-ion battery based on CPCM and topology-optimized liquid cooling. *Energy*, 136719.

[10] Zheng, Y., Che, Y., Hu, X., Sui, X., & Teodorescu, R. (2023). Sensorless temperature monitoring of lithium-ion batteries by integrating physics with machine learning. *IEEE Transactions on Transportation Electrification*, *10*(2), 2643-2652.

[11] Santos, J. E., Fox, Z. R., Mohan, A., O'Malley, D., Viswanathan, H., & Lubbers, N. (2023). Development of the Senseiver for efficient field reconstruction from sparse observations. *Nature Machine Intelligence*, *5*(11), 1317-1325.

[12] Du, H., Xu, Q., Bu, Y., Jiang, L., Zhao, C., Zhang, C., & Yan, J. (2024). Rapid prediction of structural thermal loads and temperature field based on physics and data co-driven approach under partial labeled data. *International Communications in Heat and Mass Transfer*, *159*, 108007.

[13] Jiang, L., Du, H., Bu, Y., Zhao, C., Lu, H., & Yan, J. (2024). Deep learning-based multilabel compound-fault diagnosis in centrifugal pumps. *Ocean Engineering, 314*.

[14] Du, H., Jiang, L., Zhao, C., Li, W., Bu, Y., Xu, Q., ... & Yan, J. (2025). Industrial equipment structure multivariate regression prediction via random input and hybrid temporal neural networks. *Advanced Engineering Informatics*, *64*, 103006.

[15] Narayana, K. V. L., & Kumar, V. N. (2016). Development of an intelligent

temperature transducer. *IEEE sensors journal*, *16*(12), 4696-4703.

[16] Du, H., Xu, Q., Jiang, L., Bu, Y., Li, W., & Yan, J. (2024). Stepwise identification method of thermal load for box structure based on deep learning. *Materials*, *17*(2), 357.

[17] Liu, J., Wang, F., Jiang, X., Mao, D., & Wang, X. (2024). Optimization of distributed optical fiber temperature monitoring points based on 3D temperature field reconstruction. *Thermal Science and Engineering Progress*, 53, 102741.

[18] Xiang, Y., Lin, P., Peng, H., Li, Z., Liu, Y., Qiao, Y., & Yang, Z. (2024). Optimization Method for Improving Efficiency of Thermal Field Reconstruction in Concrete Dam. *Applied Sciences (2076-3417)*, *14*(23).

[19] Carr, J. C., Beatson, R. K., Cherrie, J. B., Mitchell, T. J., Fright, W. R., McCallum, B. C., & Evans, T. R. (2001, August). Reconstruction and representation of 3D objects with radial basis functions. In *Proceedings of the 28th annual conference on Computer graphics and interactive techniques* (pp. 67-76).

[20] Yoo, D. J. (2011). Three-dimensional surface reconstruction of human bone using a B-spline based interpolation approach. *Computer-Aided Design*, *43*(8), 934-947.

[21] Feng, W., Li, Q., & Lu, Q. (2020). Force localization and reconstruction based on a novel sparse Kalman filter. *Mechanical Systems and Signal Processing*, *144*, 106890.

[22] Liang, G., Dong, F., Kolehmainen, V., Vauhkonen, M., & Ren, S. (2020). Nonstationary image reconstruction in ultrasonic transmission tomography using Kalman filter and dimension reduction. *IEEE Transactions on instrumentation and measurement*, *70*, 1-12.

[23] Protasov, A. (2017, August). Reconstruction of the thermal field image from measurements in separate points. In *2017 IEEE Microwaves, Radar and Remote Sensing Symposium (MRRS)* (pp. 89-92). IEEE.

[24] Yan, H., Lin, H., & Wang, S. (2013). 3D Temperature Field Reconstruction: A Comparison Study of Direct and Indirect Method. In *Proceedings of 2013 Chinese Intelligent Automation Conference: Intelligent Automation & Intelligent Technology and Systems* (pp. 849-857). Springer Berlin Heidelberg.

[25] Wang, Z., Wang, G., Chen, H., & Zhang, T. (2025). Temperature response correlation model between body and coolant and direct reconstruction of temperature field in lithium-ion battery pack. *Applied Thermal Engineering*, *278*, 127186.

[26] Liu, H. X., Li, M. J., Guo, J. Q., Zhang, X. K., & Hung, T. C. (2024). Temperature prediction of submerged arc furnace in ironmaking industry based on residual spatial-temporal convolutional neural network. *Energy*, *309*, 133024.

[27] Almas, M., & Sundaram, S. (2025). Integrating artificial intelligence based hybrid deep learning prediction models to estimate exergy efficiency for realistic solar photovoltaic power plants: validation with ground measurements. *Thermal Science and Engineering Progress*, 103902.

[28] Xu, M., & Chen, C. (2025). Application and research of intelligent temperature control system based on deep learning in precision manufacturing product design. *Thermal Science and Engineering Progress*, 57, 103185.

[29] Chen, Y., Chen, Q., Ma, H., Chen, S., & Fei, Q. (2025). Transfer machine learning framework for efficient full-field temperature response reconstruction of thermal protection structures with limited measurement data. *International Journal of Heat and Mass Transfer*, *242*, 126785.

[30] Yan, J., Du, H., Bu, Y., Jiang, L., Xu, Q., & Zhao, C. (2024). Data-Driven Method for Real-Time Reconstruction of the Structural Displacement Field. *Journal of Aerospace Engineering*, *37*(3), 04024028.

[31] Li, Y., Chang, J., Wang, Z., & Kong, C. (2019). Inversion and reconstruction of supersonic cascade passage flow field based on a model comprising transposed network and residual network. *Physics of Fluids*, *31*(12).

[32] Gong, T., & Wang, Y. (2025). An artificial neural network-based quadratic constitutive Reynolds stress model for separated turbulent flows using data-augmented field inversion and machine learning. *Physics of Fluids*, *37*(3).

[33] Kang, M., Nguyen, N. P., & Kwon, B. (2024). Deep learning model for rapid temperature map prediction in transient convection process using conditional generative adversarial networks. *Thermal Science and Engineering Progress*, *49*, 102477.

[34] Liu, S., Liu, C., & Hou, X. (2025). Numerical simulation and experimental study of radiative thermal environment in solid rocket motors based on Fourier feature physics-informed neural networks. *Applied Thermal Engineering*, 128001.

[35] Xie, J., Zhang, J., Cheng, Y., Zhou, J., Li, X., Li, X., & Mao, G. (2025). Real-Time prediction of wellbore temperatures in deep shale gas drilling using a combination of PINN and heat transfer models. *Applied Thermal Engineering*, 127984.

[36] Yue, L., Zihao, F., Qiang, C., Baolin, W., & Kaifa, W. (2025). Physics-informed

neural network for transient behavioral modeling of thermoelectric generators. *Applied Thermal Engineering*, 127996.

[37] Ma, H., Zhang, B., Zhang, C., & Haidn, O. J. (2021). Generative adversarial networks with physical evaluators for spray simulation of pintle injector. AIP Advances, 11(7).

[38] Raissi, M., Perdikaris, P., & Karniadakis, G. E. (2019). Physics-informed neural networks: A deep learning framework for solving forward and inverse problems involving nonlinear partial differential equations. *Journal of Computational physics*, *378*, 686-707.

[39] Lawal, Z. K., Yassin, H., Lai, D. T. C., & Che Idris, A. (2022). Physics-informed neural network (PINN) evolution and beyond: A systematic literature review and bibliometric analysis. *Big Data and Cognitive Computing*, *6*(4), 140.

[40] Ma, X., Qiu, L., Zhang, B., Wu, G., & Wang, F. (2025). Adaptive fractional physics-informed neural networks for solving forward and inverse problems of anomalous heat conduction in functionally graded materials. *International Journal of Heat and Mass Transfer*, *236*, 126393.

[41] Oldenburg, J., Borowski, F., Öner, A., Schmitz, K. P., & Stiehm, M. (2022). Geometry aware physics informed neural network surrogate for solving Navier–Stokes equation (GAPINN). *Advanced Modeling and Simulation in Engineering Sciences*, *9*(1), 8.

[42] Tian, R., Kou, P., Zhang, Y., Mei, M., Zhang, Z., & Liang, D. (2024). Residual-connected physics-informed neural network for anti-noise wind field reconstruction. *Applied Energy*, *357*, 122439.

[43] Zhang, X., Shi, J., Li, J., Huang, X., Xiao, F., Wang, Q., ... & Chen, G. (2025). Hydrogen jet and diffusion modeling by physics-informed graph neural network. *Renewable and Sustainable Energy Reviews*, *207*, 114898.

[44] Soibam, J., Aslanidou, I., Kyprianidis, K., & Fdhila, R. B. (2024). Inverse flow prediction using ensemble PINNs and uncertainty quantification. *International Journal of Heat and Mass Transfer*, *226*, 125480.

[45] Ye, S., Huang, J., Zhang, Z., Wang, Y., & Huang, C. (2025). Direct numerical simulation of natural convection based on parameter-input physics-informed neural networks. *International Journal of Heat and Mass Transfer*, *236*, 126379.

[46] Peng, J. Z., Aubry, N., Li, Y. B., Mei, M., Chen, Z. H., & Wu, W. T. (2023). Physics-informed graph convolutional neural network for modeling geometry-adaptive

steady-state natural convection. *International Journal of Heat and Mass Transfer*, *216*, 124593.

[47] Bora, A., Dai, W., Wilson, J. P., & Boyt, J. C. (2021). Neural network method for solving parabolic two-temperature microscale heat conduction in double-layered thin films exposed to ultrashort-pulsed lasers. *International Journal of Heat and Mass Transfer, 178*, 121616.

[48] Wang, Y., & Ren, Q. (2022). A versatile inversion approach for space/temperature/time-related thermal conductivity via deep learning. *International Journal of Heat and Mass Transfer, 186*, 122444.